

Discussion of the influence of turbulence models on unsteady cavitation flows past a hydrofoil

Byungjin AN*
Graduate School of Engineering,
Osaka University, Japan

Takeo KAJISHIMA
Department of Mechanical Engineering,
Osaka University, Japan

*anbj@fluid.mech.eng.osaka-u.ac.jp

ABSTRACT

A numerical simulation of two-dimensional unsteady cavitating flows around a Clark-Y 11.7% hydrofoil was carried out to assess the validity of our cavitation model and the effect of the Reynolds-averaged turbulence model. In order to achieve this objective, two kinds of numerical results were compared for various cavitation numbers and two angles of attack. One is the RANS simulation with the single-phase Baldwin-Lomax model and the other is the simulation without any explicit model for turbulence. Regardless of the use of the turbulence model, we were able to reproduce the characteristic observed in the experiment as the cavitation number decreased: a slight peak of the lift coefficient appeared just before the breakdown and the lift coefficient was kept almost constant until the breakdown, both of which are related to the length of partial cavitation. By using a RANS model, the unrealistically spiky fluctuation in the time evolution of the lift coefficient was reduced; on the other hand, the influence of essential unsteadiness of partial cavity might also be attenuated. Nonetheless, the reproduction of the phenomena improved by the simulation on the basis of a more appropriate method for single-phase turbulence.

NOMENCLATURE

f_l	Volumetric fraction of liquid phase
C_p	Pressure coefficient
C_L, C_D	Lift and drag coefficients
α	Angle of attack
p	Static pressure
p_v	Vapor pressure
$Re (= Cu_{in} / \nu_l)$	Reynolds number
σ	Cavitation number
ν_T	Eddy-viscosity coefficient
$J (= \partial x_i / \partial \xi^j)$	Jacobian of coordinate transformation
U^j	Contra-variant components of velocity
u_i	Cartesian components of velocity
u_{in}	Inlet velocity
x_i	Cartesian coordinate
ξ^j	Curvilinear coordinate

1. INTRODUCTION

For the purpose of prediction and control of cavitating flows in high-speed hydro-machineries, various cavitation models and numerical methods have been developed. In the Turbomachinery Society of Japan, an industry-university collaborative research project [1] has been conducted to improve our understanding and the reliability of current models for the use of cavitating flows. However, for hydrofoil performance, the agreement between numerical results and experimental data was not always satisfactory. In the project, several causes were pointed out [1] for the discrepancies including but not limited to: cavitation model, turbulence model, mesh resolution and boundary conditions.

In this study, numerical analysis for two-dimensional (2D) unsteady cavitating flows around a Clark-Y hydrofoil was performed to assess the validity of our cavitation model and the effect of the Reynolds-averaged turbulence model. In our simulation, the cavitation model [2] is the modification of Chen-Heister model [3] and the turbulence model is the standard Baldwin-Lomax model [4]. Then, we will discuss the influence of the treatment of unsteadiness on the numerical results of hydrofoil performance.

2. OUTLINE OF COMPUTATION

2.1 Computational setup

In this study, the flow around a two-dimensional hydrofoil of Clark-Y 11.7% is dealt with. The computational domain is C-type around the cross-section of the hydrofoil and the curvilinear coordinate is used for the generation of structured mesh as shown Figure 1. The number of grid points is 240×90 and the size of domain is $10C \times 10C$, where C is the chord length. The grid near the hydrofoil is shown in Figure 2. Note that the angle between the chord and the quasi-plane of the lower side is approximately 2 degrees. The Reynolds number which is based on the chord length C and the mainstream velocity u_{in} is $Re = 6 \times 10^5$, and the time increment of the computation is $\Delta t = 5 \times 10^{-5}$.

The uniform inflow boundary condition was set up at the semicircle of radius $5C$ from the tailing edge. The velocity gradient of the normal components of the inflow boundary is 0.

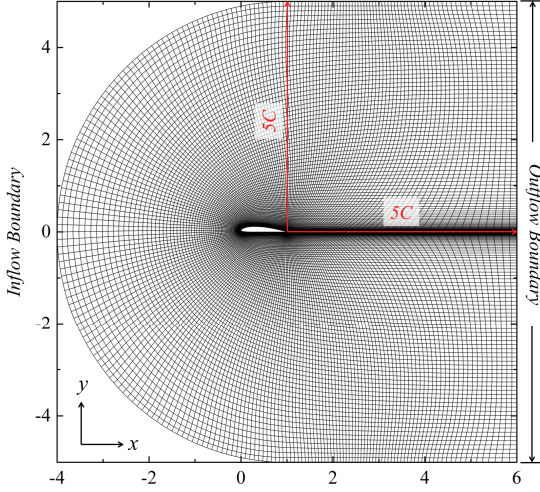


Figure 1: Computational domain of C-type around a 2D hydrofoil (Clark-Y 11.7%)

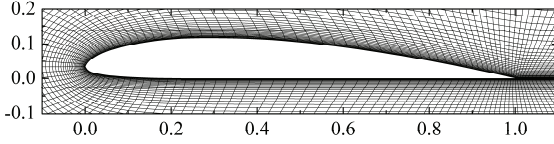


Figure 2: Grid around a 2D hydrofoil (Clark-Y 11.7%)

At the far (top and bottom) boundaries, the normal components of the boundaries of the velocity and the pressure gradient are 0. At the outflow boundary, the pressure is fixed at 0 and the velocity gradient of the normal components of boundary is set as 0. The non-slip boundary condition is applied at the hydrofoil surface.

2.2 Governing equations

Hereafter, all variables are non-dimensionalized by a chord length of hydrofoil C , uniform inflow velocity u_∞ and the liquid density ρ_L .

The isothermal field is assumed. Thus the governing equations are the conservation laws of mass and momentum of the homogeneous mixture of liquid and vapor. The mass conservation equation can be expressed by the liquid volumetric fraction f_L as follows:

$$\frac{Df_L}{Dt} + f_L \frac{1}{J} \frac{\partial (JU)^j}{\partial \xi^j} = 0 \quad (1)$$

The momentum equation can be written as follows:

$$\begin{aligned} \frac{\partial u_i}{\partial t} + U^j \frac{\partial u_i}{\partial \xi^j} = & -\frac{1}{f_L} \frac{\partial \xi^k}{\partial x_i} \frac{\partial p}{\partial \xi^k} \\ & + \frac{1}{J} \frac{\partial}{\partial \xi^k} \left\{ \left(\frac{1}{Re} + v_T \right) J \frac{\partial \xi^k}{\partial x_j} \frac{\partial u_i}{\partial x_j} \right\} \end{aligned} \quad (2)$$

where, x_i is the Cartesian coordinate, ξ^j is the curvilinear

coordinate and J is the Jacobian of the coordinate transformation. u_{in} is x_i direction component of the velocity, U^j is the contravariant velocity of direction ξ^j . Re is the Reynolds number; v_T is the eddy-viscosity coefficient which is non-dimensionalized.

For the cavitating flow, the eddy-viscosity coefficient by the Baldwin-Lomax turbulence model [4] for a single-phase flow is extensionally used.

2.3 Cavitation model

The cavitation model is the source term model which is the modification [2] of the Chen-Heister model [3]. The change of the liquid volumetric fraction f_L is represented by:

$$\frac{Df_L}{Dt} = \{C_1(1-f_L) + C_0\}(p - p_v) \quad (3)$$

This equation means that the cavitation region will expand under the condition $p < p_v$, whereas it will contract in the region of $p > p_v$. The model constants are $C_1 = 1000$ and $C_0 = 1$. The saturated vapor pressure p_v is given from the cavitation number:

$$\sigma = \frac{p_\infty - p_v}{\frac{1}{2} \rho_L u_\infty^2} \quad (4)$$

using a reference pressure p_∞ fixed in the outflow boundary of downstream.

2.4 Outline of computational method

The time marching procedure is based on the fractional step method. The 2nd order Adams-Bashforth method is used for the convective and viscous terms, and backward Euler method is used for the pressure term and the continuity equation. The viscous term is discretized with central differences of the 2nd order accuracy. The QUICKEST [5] is applied for the convective term.

3. RESULTS

The cavitating flow around the Clark-Y hydrofoil under the condition in our study is essentially unsteady, three-dimensional and turbulent. But, considering the rather practical approach, we investigate the ability of two-dimensional simulation in this work. As for the turbulence model, the time-scale relation between unsteady cavitation and turbulence phenomena are generally unknown. In addition, to the best of our knowledge, the turbulence model for the Reynolds-averaged numerical simulation (RANS) or large-eddy simulation (LES) has not yet been established to take into account the cavitation. We think the RANS model is desirable at this stage because LES is meaningless in the two-dimensional simulation. Thus we adopt the Baldwin-Lomax model, which is generally used for steady flow of single-phase fluid. Since the time-marching term is included in the governing equation, some sort of unsteadiness is expected to be reproduced.

In this section, we compare two kinds of numerical simulations. One is the RANS simulation with the single-phase Baldwin-Lomax model and the other is the simulation without any explicit model for turbulence. In both of simulations,

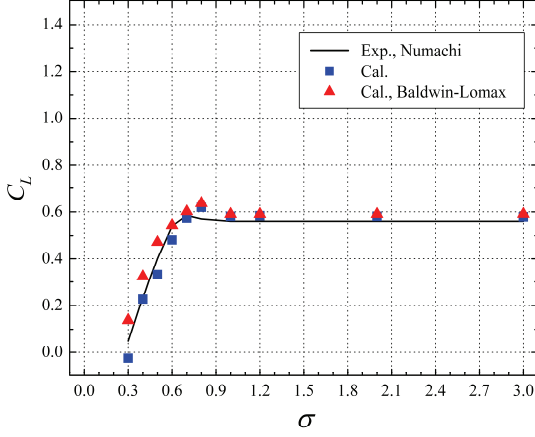


Figure 3: Variations of lift coefficients at $\alpha = 2^\circ$

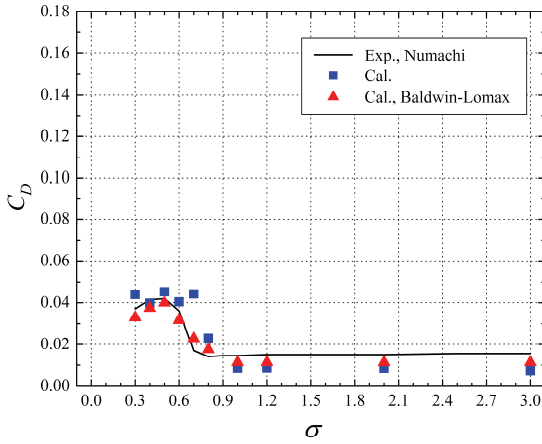


Figure 4: Variations of drag coefficients at $\alpha = 2^\circ$

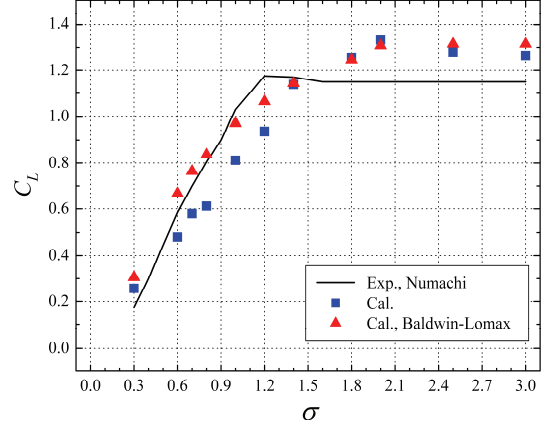


Figure 5: Variations of drag coefficients at $\alpha = 8^\circ$

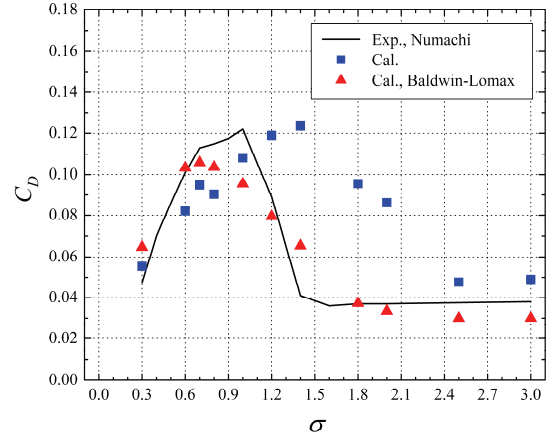


Figure 6: Variations of drag coefficients at $\alpha = 8^\circ$

the QUICKEST method is used for the numerical stability. Though the physical meaning of the QUICKEST method is actually not clear, it might dump numerical wiggles and natural turbulence inevitably. In the sense that our computation is two-dimensional and that it includes a numerical dumping, we do not term the direct numerical simulation (DNS) for the case without an explicit turbulence model. Hereafter, in the presentation of our results, we just indicate by ‘with’ or ‘without’ of the turbulence model.

A series of numerical simulations were performed to assess the validity of our cavitation model, the effect of the turbulence model for several cavitation numbers and the angle of attack, which are 2 and 8 degrees for Clark-Y 11.7% hydrofoil. The results were compared with experimental results by Numachi [6]. One should note that the experiment was conducted in a cavitation tunnel of spanwise width C and height about $2.7C$. Thus the cross-sectional domain condition is not equivalent to our case of Figure 1. The difference may become influential in the case of a higher angle of attack.

Figure 3 shows the results of the lift coefficient (C_L) for several cavitation numbers when the angle of attack is 2 degrees. From the results without the turbulence model expressed in a blue square and with the turbulence model expressed in a red

triangle, the tendency of the performance curve approximately corresponds with experimental data [6] expressed with the black solid line. Furthermore, we were able to reproduce the characteristic that the peak of the C_L appears just before the breakdown takes place as the cavitation number decreases. In the range of the single phase flow field where the cavitation number is higher than 1.2, there are almost no differences between the results of simulations with or without the turbulence model. However, the difference becomes pronounced for cavitation numbers lower than 1.2.

Figure 4 shows the results of the drag coefficient (C_D) for the angle of attack of 2 degrees. In the condition that cavitation does not occur, the calculation underestimated the frictional resistance in comparison with the experimental result. A two-layer model, which consists of viscous sublayer and log layer, was applied to estimate the frictional stress. This may include some quantitative uncertainty. At any rate, the increase of the frictional resistance by cavitation is reproduced sufficiently.

Figure 5 and 6 shows the results of C_L and C_D as functions of the cavitation number σ when the attack angle is 8 degrees. From figure 5, C_L of the experiment starts to decrease at cavitation number 1.2 while C_L of the simulation starts to decrease at 2.0. We believe the discrepancy may have been

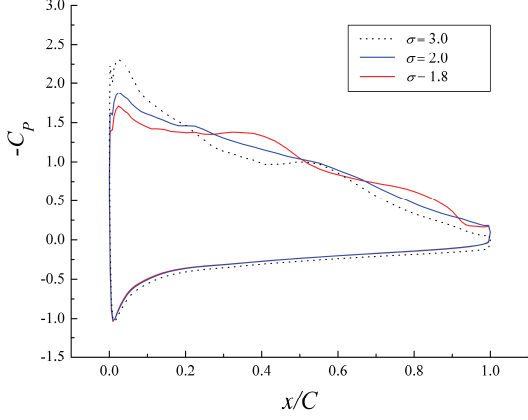


Figure 7: Comparisons of static pressure around hydrofoil without using turbulence model at $\alpha = 8^\circ$

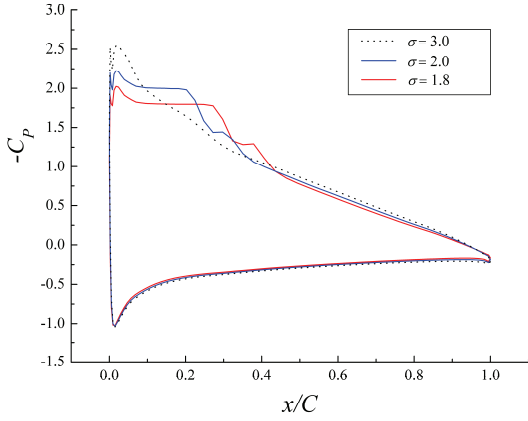


Figure 8: Comparisons of static pressure around hydrofoil using turbulence model at $\alpha = 8^\circ$

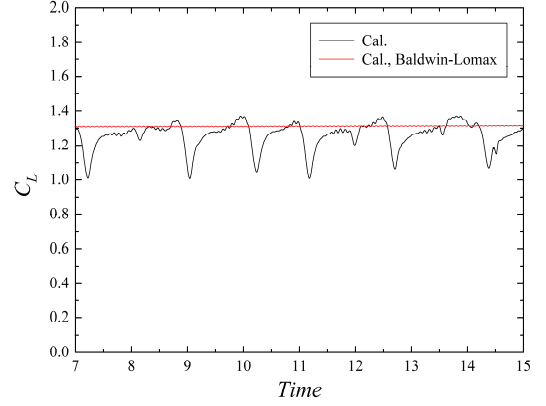


Figure 9: Time evolution of lift coefficients at $\alpha = 8^\circ$, $\sigma = 3.0$

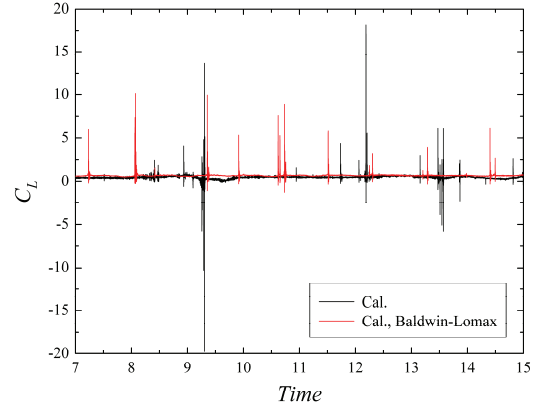


Figure 10: Time evolution of lift coefficients at $\alpha = 8^\circ$, $\sigma = 0.6$

mainly due to the difference in the domain size and the boundary conditions between our computation and the experiment. Nonetheless, we were able to confirm the qualitative characteristic that the peak of the C_L appears just before the breakdown when σ is decreased.

As shown in Figure 6, C_D for the simulation without the turbulence model increases with σ in the range of $\sigma < 1.5$. Particularly, in the range of $0.6 < \sigma < 1.5$, this tendency is opposite to that by the Baldwin-Lomax model. This range corresponds to the underestimation of C_L by the simulation without the turbulence model as shown in Figure 5. It is probably because the unsteady massive separations are likely to be caused by the absence of turbulence viscosity. Overall, the addition of RANS reproduced better agreement with the experimental data. But it does not simply indicate the appropriateness of the Baldwin-Lomax model, because the physics involved in the unsteady cavitating flow are different from the background of the model.

The profile of the pressure coefficient along the hydrofoil was informative to elucidate the breakdown characteristics.

Figure 7 compares the profiles of static pressure coefficient

$$C_p = \frac{p - p_\infty}{\frac{1}{2} \rho_L u_\infty^2} \quad (6)$$

on the hydrofoil at various cavitation numbers without using the turbulence model. Figure 8 compares C_p on the hydrofoil using the turbulence model. For the case of attack angle 8 degrees, the maximum value of $-C_p$ is about 2.3 (Fig. 7) and 2.5 (Fig. 8). This indicates that the cavitation takes place at the cavitation number lower than these values, because of the definition of σ . It also means that $-C_p$ cannot be higher than σ . These limitations suggest the decrease in C_L . However, as shown in Figure 5, C_L values increase slightly with the decrease of σ from 3 to 2. This can be explained mainly by the increase of $-C_p$ in the other part of the suction side, which is the elongation of the sheet cavitation region. Such a tendency is depicted by the expansion of the region of $-C_p$ nearly equal to σ . This tendency is more visible in Figure 8 in comparison with that in Figure 7. On the other hand, in Figure 7, the $-C_p$ profile is undulated in the whole region of the suction side. It may be due to the unsteady

massive separation in the numerical result obtained without the RANS model. Therefore, although the two results shown in Figure 5 are similar, the cause of C_L breakdown characteristic is qualitatively different. Of course the Baldwin-Lomax model is not complete for cavitating flows, so we think such numerical simulations should be prepared on the basis of a more reasonably reproduced turbulent flow field.

Figure 9 shows the time evolution of lift coefficient for the angle of attack $\alpha = 8^\circ$ and the cavitation number $\sigma = 3.0$, which is considered as the non-cavitating flows condition. In the case without the explicit turbulence model, C_L becomes unsteady but it is not fully random. The time-evolution patterns suggest a kind of organized motion. The period is not so clear but it is approximately unity (a non-dimensional time). On the other hand, C_L becomes steady by adding the Baldwin-Lomax turbulence model, as expected. In Figure 10, for the same angle of attack and cavitation number $\sigma = 0.6$, the time-evolution of C_L shows a spiky pattern. The peak value of C_L has the different order of magnitude in comparison with the time-average. Especially, in the result without the turbulence model, the negative peak seems unrealistically large. But one may keep in mind that the contribution of these spiky fluctuations is negligible in the time average. Except for these spikes, C_L by the Baldwin-Lomax model is almost constant but C_L by the method without turbulence model is undulated. The latter indicate a decrease of C_L for a while, which may be caused by the massive separation. From the viewpoint of spiky and mild unsteady patterns, we think the Baldwin-Lomax model improved the reproduction of unsteady characteristics.

4. CONCLUSION

The numerical analysis for two-dimensional unsteady cavitating flows around a Clark-Y 11.7% hydrofoil was performed to assess the validity of our cavitation model and the effect of the Reynolds-averaged turbulence model. We compared two kinds of numerical results for various cavitation numbers at the two angles of attack, 2 degrees and 8 degrees. One is the RANS simulation with the single-phase Baldwin-Lomax model and the other is the simulation without any explicit model for turbulence. As the result, we were able to reproduce the characteristic that the peak of the lift coefficient appears just before the breakdown regardless of the use of the turbulence model. This phenomenon was explained as a result of profiles of the pressure coefficient along the hydrofoil surface. Namely, it is related to the length of partial cavitation. Besides, when the turbulence model is adapted, the tendency is more remarkable in comparison with the case of without that. From the result of the time evolution of lift coefficient, the unrealistic spiky fluctuation, which appears in the condition of non-cavitating flows, was reduced by using a RANS model. However, there is a problem that the essential unsteadiness of partial cavity might also be attenuated.

We think that the adoption of the RANS will improve the agreement of numerical and experimental results. However it does not simply indicate the appropriateness of the Baldwin-Lomax model, because the physics involved in the unsteady cavitating flow are not included in the concept of the model.

Thus, we also think that the three-dimensionality and the unsteadiness should be taken into account to reproduce the cavitating flows quantitatively even in the two-dimensional simulation.

ACKNOWLEDGMENTS

The first author would like to acknowledge the Ministry of Education, Culture, Sports, Science and Technology (MEXT) - Japan for financial support through the scholarship program. This work was partially supported by a Grant-in-Aid for Scientific Research No. 23360085 from MEXT of Japan. A part of this study is in association with the industry-university collaborative research project on the CFD of cavitating flows organized by Turbomachinery Society of Japan. The discussion in the group was very informative for the present study.

REFERENCES

- [1] Kato, C., 2011, "Industry-University Collaborative Project on Numerical Predictions of Cavitating Flows in Hydraulic Machinery," *Proc. 4th ASME-JSME-KSME Joint Fluids Engineering Conference (AJK2011)*, Hamamatsu, JAPAN.
- [2] Okita, K. and Kajishima, T., 2000, "Numerical investigation of unsteady cavitating flow around a rectangular prism," *Proc. 4th JSME-KSME Thermal Engineering Conference, Kobe*, Vol. 2, pp. 571-576.
- [3] Chen, Y., and Heister, S., 1995, Two-phase modeling of cavitating flows, *Computers & Fluids*, Vol. 24, No. 7, pp. 799-809.
- [4] Baldwin, B. S., and Lomax H., 1978, "Thin layer approximation and algebraic model for separated turbulent flows," *AIAA 16th Aerospace Sciences Meeting*, No. 78-257.
- [5] Leonard, B. P., 1979, "A stable and accurate convective modelling procedure based on quadratic upstream interpolation," *Computer Method in Applied Mechanics and Engineering*, Vol. 19, pp. 59-98.
- [6] Numachi, F., Tsunoda, K., and Chida, I., 1948, "Cavitation tests on six profiles for blade elements," *Journal of the Japan Society of Mechanical Engineers*, Vol. 17, No. 60, pp. 1-5.

Unsteady Cavitation around a Plano-Convex Hydrofoil with Flow visualization by Using Liquid Nitrogen and Water

Yutaka Ito*/Tokyo Institute of Technology

Hiroshi Yamauchi / Tokyo Institute of Technology

Takao Nagasaki / Tokyo Institute of Technology

ito@es.titech.ac.jp

ABSTRACT

Cavitation around a Plano-convex hydrofoil in a channel flow with various angle of attack -8° to $+8^\circ$, Reynolds number 0.24×10^6 to 2.3×10^6 , and cavitation number -1.1 to 85.1 was observed by a blow-down type cavitation tunnel with flow visualization. Liquid nitrogen and hot water was employed as working fluids. The following three are found by experimental results. 1: Cavitation patterns can be sorted into a partial cavitation, a shear cavitation, a cloud cavitation, and a super cavitation in the same way as Le's water free surface flow although our experiments were performed in liquid nitrogen and water channel flows. 2: A cavitation patterns map can be made on a chart of degree of subcool versus dynamic pressure for a wide range of Reynolds number in cases of specified angle of attack and hydrofoil chord length. 3: Only a cloud cavitation is unsteady one with large scale decay of the part of the cavitation. Even though the part of the cavity exists in a range of $0.6 \leq L/L_C \leq 1.2$ for a moment at least, the cavity is unsteady and a cloud cavitation occurs.

1. INTRODUCTION

Cavitation is one of the most difficult problems to be surmounted in the development of turbo-pumps for liquid fuel rocket engines. Because high performance engines require high combustion pressure, their turbo-pumps have to operate at high rotating speed. The best performance of the pump can be obtained when cavitation occurs stably at high rotating speed. Therefore it is necessary to allow controllable cavitation to form in the pump. Current large size main engines utilize cryogenics as a fuel and an oxidizer, for examples, liquid hydrogen and liquid oxygen for U.S. SSME, Japan's LE-7A, Europe's Valcain2, and U.S. RS-68, or kerosene and liquid oxygen for Russia's RD-170/180/190. Because cryogenics have thermodynamic features called "thermodynamic effects" different from ordinary fluids like water, cryogenic cavitation is complicated, and it is hard to control cryogenic cavitation without deeply understanding its behavior and its influences on the pump performance. Although conventional design methods of pumps against cavitation are available for water, experiments on cryogenic cavitation with flow visualization play a very important role in clarifying the features of cryogenic cavitation at the moment, and in getting knowledge of how to allow controllable cavitation in the near future.

Unsteady phenomena of cavitation around a high-speed rotating impeller like a turbo-pump can be roughly sorted into a phenomenon based on resonance of a whole piping system like cavitation surge, a phenomenon synchronized with rotating impellers like rotating cavitation, and a phenomenon of fluid-structure interaction like a Karman vortex even in the case of no rotating hydrofoil. Practical phenomena are very complicated because they are usually combined with each other, and/or there is an additional interaction with their mounting system like Pogo oscillation. This study is focused on interaction between cavitation and a static two-dimensional hydrofoil as basis for understanding unsteady cavitation around a rotating impeller.

Although there are of course a huge number of two-dimensional hydrofoil shapes, a plano-convex hydrofoil is a good choice. It has a very simple shape. Its one surface is plane, and the other is convex. Its thickness is thin compared with its chord length. Its leading and trailing edges are sharp. These features are very similar to practical turbo-pump impellers. Therefore, a lot of researchers such as Wade & Acosta (1966) [1], Le et al. (1993) [2], and so on, employed the plano-convex hydrofoil as a test model.

Wade & Acosta carried out a study on water cavitation around a plano-convex hydrofoil with flow visualization as well as measurements of lift and drag coefficients. They observed a cavitation forming on the hydrofoil, and measured the cavitation length. They also distinguished whether the cavitation is steady or unsteady. They pointed out that the cavitation oscillates when the cavitation length is about 60% to 120% to the hydrofoil chord length. They concluded that the cavitation behavior around the plano-convex hydrofoil was able to be divided into three regimes: a partial cavitation region, a super cavitation region, and an unsteady cavitation region existing between the former two regions. They mentioned that the effect of the cavitation tunnel boundaries on the unsteady cavitation should be clarified, and experiments of the hydrofoil submerged in a liquid flow with free surface were also required to remove the effect of tunnel boundaries.

Le et al. conducted a visualization study on water cavitation around a plano-convex hydrofoil. Their water tunnel set in a horizontal direction, and it had free surface above the plane surface of the plano-convex hydrofoil because they always put the plane surface upward. They measured pressure distribution on the plane surface. They made a map of cavitation patterns

distribution on a chart of cavitation number σ versus angle of attack AOA at Reynolds number $Re=2$ million. They classified cavitation patterns into no cavitation, a partial cavitation, a shear cavitation, a periodical shedding cavitation, and a super cavitation. It was verified that the periodical shedding cavitation occurred in a free surface flow. They discussed that a threshold of open or close cavitation is relating to the excess of pressure coefficient C_p on the hydrofoil in a cavitation compared with a negative inlet cavitation number $-\sigma_{in}$.

Callenaere (2001) [3] used a diverging step instead of a hydrofoil in a water tunnel to investigate the instability of a partial cavitation. He revealed that an adverse pressure gradient played an important role to trigger the cloud cavitation shedding, and a cavitation thickness comparable to the size of an adverse flow region was required to make the cloud cavitation shedding. These two factors, the adverse pressure gradient and comparable cavitation thickness, are keys to understand unsteady cavitation around hydrofoils.

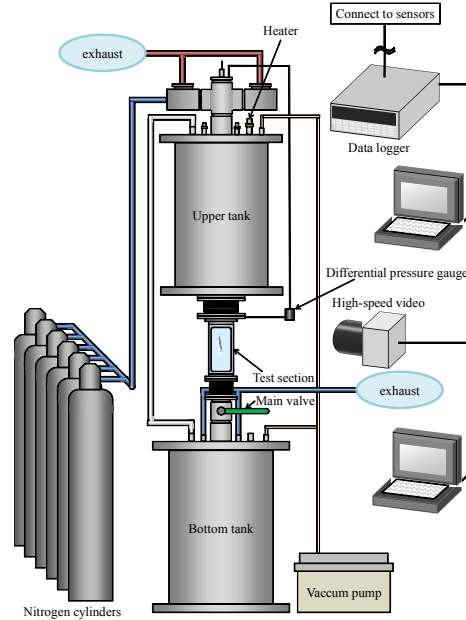
Furthermore, we must pay our attention to cryogenic working fluids. It has been known in a pump field that a pump using cryogen resists cavitation breakdown until the lesser inlet cavitation number compared with the same pump using water (reported by Stahl et al. (1956) [4], Salemann (1959) [5], Stepanoff (1961) [6], Spraker (1965) [7], Meng (1968) [8], etc.). Visualization studies on cryogenic cavitation are required because they are useful to deeply understanding a mechanism of cryogenic unsteady cavitation. However visualization for cryogenic cavitation is very difficult to make a test facility. Some cryogenic experiments have been reported for various flow configurations. Hord (1973) [9] performed experimental studies with flow visualization on a cryogenic cavitating flow

around a two-dimensional symmetric thick hydrofoil by using liquid nitrogen and liquid hydrogen. Thereafter, in order to investigate a high-speed choked flow of liquid nitrogen, liquid oxygen and liquid methane with cavitation, experiments with three nozzles of different shape were carried out by Simoneau & Hendricks (1979) [10], who made no effort to visualize the flow patterns. Several U.S. groups (1988-1994) [11-14] reported on a subsonic flow of liquid helium. However measurements were made only for pressure or mass flow rate, not for flow visualization. There have been only a few studies to visualize cryogenic cavitation, because of difficulty in the experiments. Hori et. al. (2000) [15] performed visualized experiments on the liquid nitrogen cavitating flow by employing the same nozzle profile as Simoneau & Hendricks. Ishii & Murakami (2003) [16] reported helium I and II flows in a nozzle with flow visualization successfully.

The objective of the present study is to elucidate the distinction for unsteady cavitation on the hydrofoil in a comparative way of flow visualization between cryogenic liquid nitrogen and ordinary water. The authors (2005, 2009) [17, 18] reported cavitation flow patterns on the plano-convex hydrofoil using liquid nitrogen and water in a cavitation tunnel as shown at the left in Fig.1. Unsteady cavitation was observed as a cloud cavitation shedding from the hydrofoil surface. The features of cloud cavitation shedding are different in the case of the positive AOA and negative AOA , which is defined by the angle between the approaching flow and the plane surface of the plano-convex hydrofoil (see the right on Fig. 2). Therefore, in the present study, liquid nitrogen experiments and water experiments were performed with emphasis on a cloud cavitation shedding for the cases of various AOA , as well as various σ and Re .



Cavitation tunnel for either liquid nitrogen and water



Measurement system

Fig.1 Test facility

2. EXPERIMENTAL APPARATUS AND PROCEDURES

In order to investigate the difference between cryogenic cavitation and ordinary fluid cavitation, liquid nitrogen as cryogen and water as ordinary fluid were employed because of easy handling and affordability. The experiments were conducted using a cryogenic cavitation tunnel of a blowdown type as shown at the left in Fig. 1. This tunnel has 100L upper and 120L lower tanks for liquid nitrogen and water. A test section, 288mm in length, 60mm in width, and 20mm in depth, with flow visualization was set between the tanks. A Plano-convex hydrofoil was prepared, which was homothetic with the hydrofoil used by Le et al. (1993) [2], and its scale was 3/10. Its chord length L_C , radius of the convex surface, and thickness were 60mm, 78mm, and 6mm, respectively. The angle of their leading and trailing edges was 22.6° . In addition, the channel width W was varied into 30mm by inserting blocks in the channel. AOA was set at -8° , -4° , 0° , $+4^\circ$, and $+8^\circ$. Ten combinations of W and AOA were employed, and two examples are shown at the left in Fig 2.

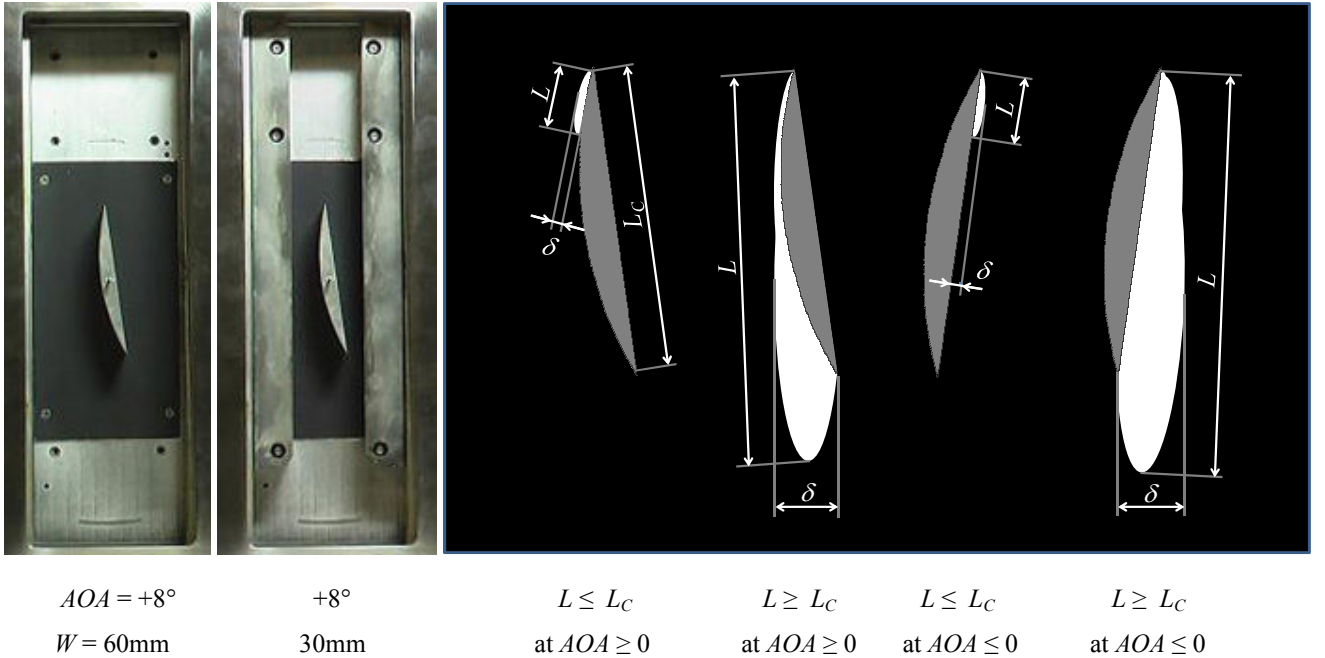
The right in Fig.1 shows measurement system of the test facility. Inlet velocity u_{in} , inlet temperature T_{in} , and inlet pressure P_{in} were varied to control cavitation number

$$\sigma = \frac{P_{in} - P_{sat}}{\frac{1}{2} \rho u_{in}^2},$$

for the inlet condition, where P_{sat} and ρ are saturation pressure and liquid density, respectively. u_{in} was altered by the pressure in the upper tank, which was pressurized by high-pressure gaseous nitrogen. u_{in} was evaluated by measurement of liquid

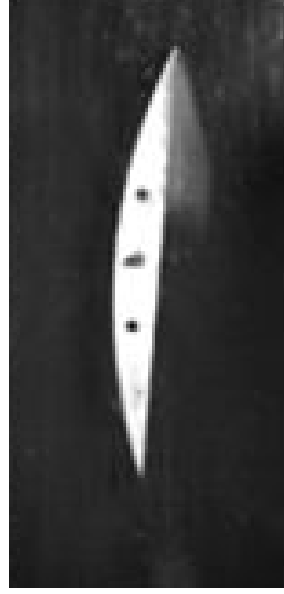
level in the upper tank using a differential pressure gage. T_{in} was set with an electric heater in water cases. In liquid nitrogen cases, heat inflow from the surroundings was balanced by evacuating the upper tank until a desired saturation temperature and pressure were achieved. This method can reduce the liquid nitrogen temperature 5K below the saturation temperature of 77.3K at atmospheric pressure. P_{in} was measured at 60mm upstream, and T_{in} was done at 67mm upstream from the center of the hydrofoil. Pressure was monitored by an electronic pressure gage, and temperature was measured by a resistance temperature detector RTD. Because the valve always opened at the outlet pipe from the lower tank to the atmosphere, therefore the backpressure in the lower tank was kept almost at the atmosphere pressure. In addition, there were two pressure taps on the convex surface of the hydrofoil. They were located at 9mm upstream (P_{up}) and downstream (P_{down}) from the center of the hydrofoil. Flow pattern of cavitation was recorded using an ordinary digital video camera and a high-speed video camera. Their recording rates were 30 and 1000/2000/5000 frames per second, respectively. A trigger signal of the high-speed video camera, u_{in} , T_{in} and the other pressure signals were recorded by a data logger and PC.

Cavitation length L , cavitation thickness δ were obtained by high-speed video camera as shown at the right in Fig.2. L is defined as a distance in a straight line from the cavitation inception point to the end of cavitation. These data have some perturbations even in cases of steady cavitation (whose definition will be stated in chapter 5). Then, both the maximum and the minimum values were recorded for these two quantities.



where, AOA : angle of attack, W : channel width, L : cavity length, δ : cavity thickness, and L_C : chord length of the hydrofoil

Fig.2 Examples of test sections, and definitions of cavity length and thickness



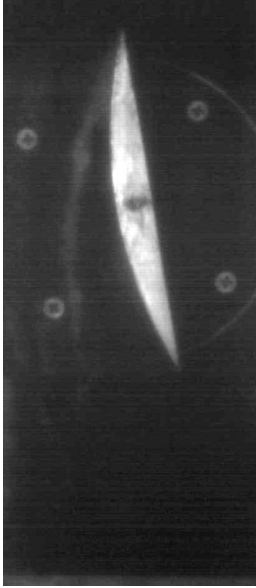
$\text{LN}_2 \text{ AOA} = 4^\circ \quad T_{in} = -194.72^\circ\text{C}$ $\text{LN}_2 \text{ AOA} = -4^\circ \quad T_{in} = -196.51^\circ\text{C}$
 $\text{Re} = 3.31 \times 10^6 \quad \sigma = 0.346$ $\text{Re} = 2.77 \times 10^6 \quad \sigma = 0.678$
 $L_C = 60\text{mm} \quad W = 60\text{mm} \text{ (V307)}$ $L_C = 60\text{mm} \quad W = 60\text{mm} \text{ (V318)}$

Fig.3 Snapshot of a partial cavitation

3. CAVITATION PATTERNS

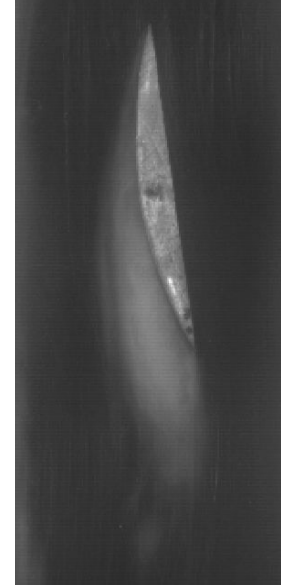
Cavitation patterns can be sorted into no cavitation, a partial cavitation, a shear cavitation, a cloud cavitation, and a super cavitation in the same way as Le et al. (1993) [2]. Figure 3 shows examples of a partial cavitation. A partial cavitation is a phenomenon that cavitation steadily exists on the hydrofoil, and the cavitation region closes on the hydrofoil. Figure 4 shows examples of a shear cavitation. A shear cavitation is a phenomenon that cavitation steadily exists at the shear region on the outer edge of the separation region. It also seems to correspond to the outer edge of the cloud cavitation. Figure 5 shows an example of a super cavitation. A super cavitation is a phenomenon that cavitation steadily covers the whole hydrofoil surface, and the end of the cavitation region is located downward of the trailing edge of the hydrofoil. Sometimes, the end of the cavitation region exceeds not only the recording area of the high-speed video camera but also the view window of the test section. Therefore it is hard to know the accurate length of a super cavitation. Figures 6 and 7 show examples of a cloud cavitation. A cloud cavitation is an unsteady phenomenon that the whole or the latter part of cavitation region are rotated and departed from the hydrofoil surface.

Although Le et al. observed cavitation patterns using a plano-convex hydrofoil in a free surface water flow, the same pattern of a cloud cavitation was observed in either liquid nitrogen and water flows in the closed cavitation tunnel. It results that this unsteadiness is derived from a hydrofoil nature not from a system instability or boundaries natures that Wade & Acosta (1966) [1] worried.



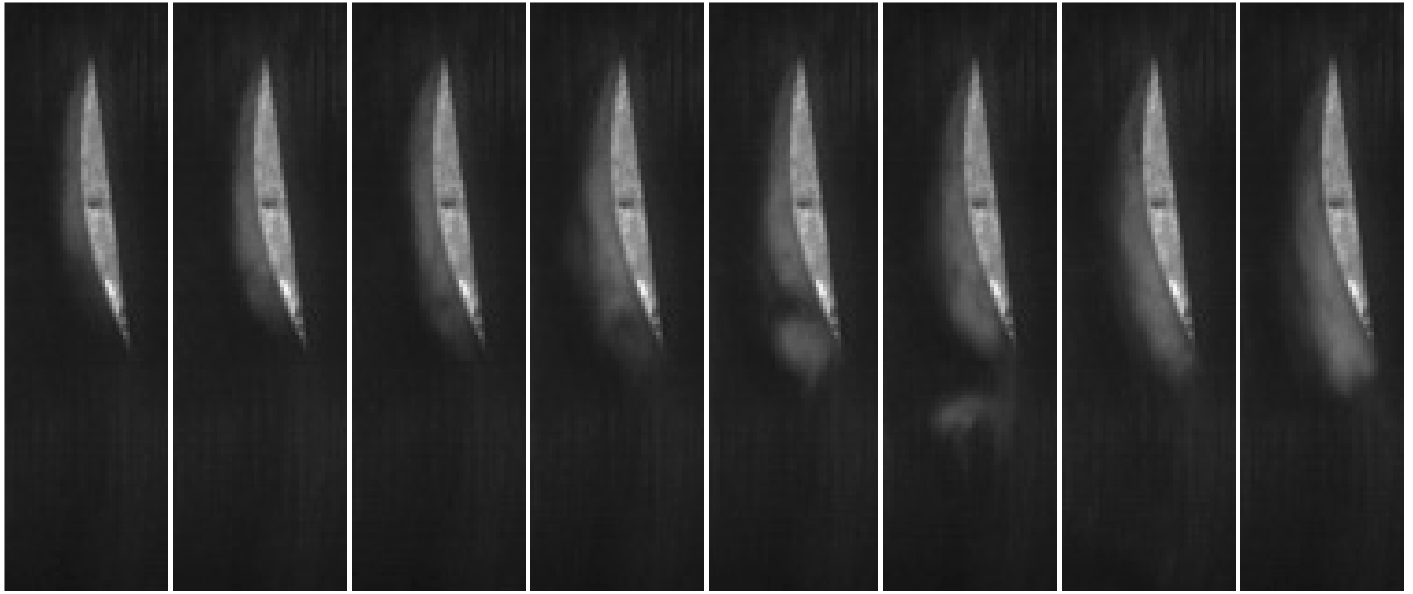
$\text{LN}_2 \text{ AOA} = 8^\circ \quad T_{in} = -196.26^\circ\text{C}$ $\text{LN}_2 \text{ AOA} = -4^\circ \quad T_{in} = -196.75^\circ\text{C}$
 $\text{Re} = 0.934 \times 10^6 \quad \sigma = 3.888$ $\text{Re} = 2.59 \times 10^6 \quad \sigma = 0.625$
 $L_C = 60\text{mm} \quad W = 60\text{mm} \text{ (N132)}$ $L_C = 60\text{mm} \quad W = 60\text{mm} \text{ (V316)}$

Fig.4 Snapshot of a shear cavitation



$\text{LN}_2 \text{ AOA} = 8^\circ \quad T_{in} = -196.26^\circ\text{C}$
 $\text{Re} = 3.22 \times 10^6 \quad \sigma = 0.473$
 $L_C = 60\text{mm} \quad W = 60\text{mm} \text{ (V127)}$

Fig.5 Snapshot of a super cavitation



$t = 0$ msec

4 msec

8 msec

12 msec

16 msec

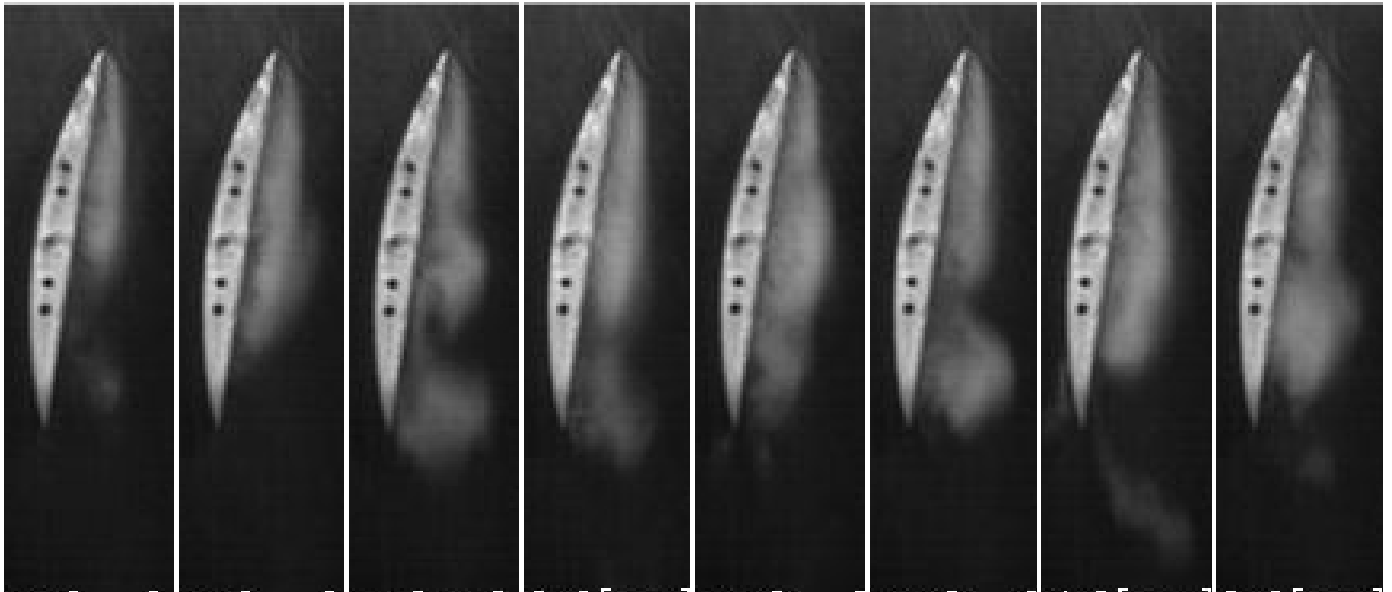
20 msec

24 msec

28 msec

LN_2 $AOA = +8^\circ$ $T_{in} = -196.41^\circ\text{C}$ $Re = 2.61 \times 10^6$ $\sigma = 0.804$ $L_C = 60\text{mm}$ $W = 60\text{mm}$ (Y130)

Fig.6 Snapshots of a cloud cavitation



$t = 0$ msec

4 msec

8 msec

12 msec

16 msec

20 msec

24 msec

28 msec

LN_2 $AOA = -8^\circ$ $T_{in} = -196.36^\circ\text{C}$ $Re = 3.29 \times 10^6$ $\sigma = 0.637$ $L_C = 60\text{mm}$ $W = 60\text{mm}$ (Y283)

Fig.7 Snapshots of a cloud cavitation

4. CAVITATION PATTERNS DISTRIBUTION

Le et al. (1993) [2] made a clear map of cavitation patterns distribution on a chart of cavitation number versus angle of attack AOA at Reynolds number $Re = 2$ million at a certain ambient temperature (They did not say about any temperature conditions, but Reynolds number is 10^6 at flow velocity 10m/s. Therefore working fluid may be water at about an ambient temperature). However, a clear map cannot be made when data have a wide range of Reynolds number.

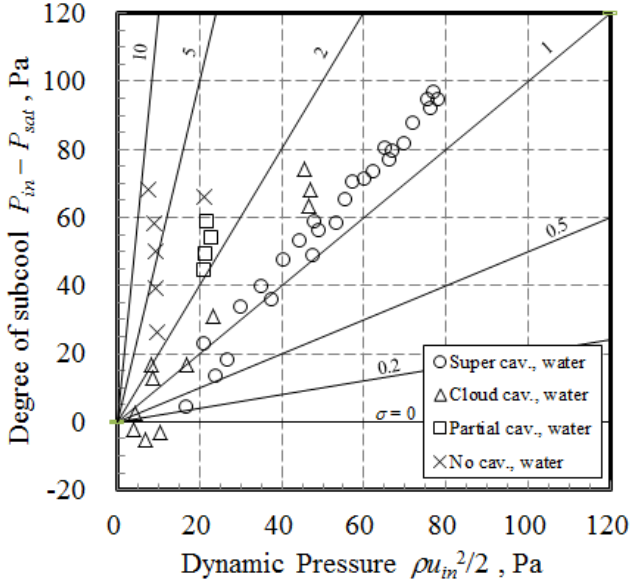
First, let us focus on water results on $L_C = 60$ mm hydrofoil in $W = 30$ mm channel at $AOA = 8^\circ$. No cavitation occurs above $\sigma \approx 2.8$. A partial cavitation is observed at $2.1 < \sigma < 2.7$. A cloud cavitation is found at $-0.8 < \sigma < 2.0$. A super cavitation is detected at $0.3 < \sigma < 1.3$. Thus, there are some clear thresholds, which are between no and a partial cavitations, and between a partial and a cloud cavitations. However, a cloud and a super cavitations mix in the region of $0.3 < \sigma < 1.3$. Therefore, cavitation patterns distribution cannot be sorted only by cavitation number in cases of a wide range of Reynolds numbers $0.24 \times 10^6 < Re < 2.3 \times 10^6$.

Whereat, experimental results is plotted on the chart, whose vertical axis is degree of subcool $P_{in} - P_{sat}$ and horizontal axis is dynamic pressure $\rho u_{in}^2/2$, as shown at the left in Fig 8. The former as numerator and the latter as denominator consist of cavitation number. Therefore, σ contours are expressed as straight lines through the origin in these figures. The horizontal line corresponds to $\sigma = 0$, and the vertical line is equivalent to $\sigma = \infty$.

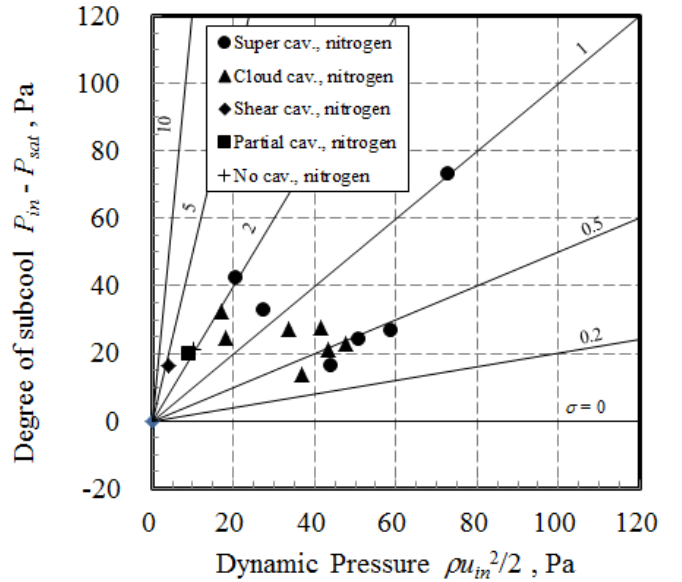
The figure indicates, for example in the region of $0.3 < \sigma < 1.3$, which is the mixed region of a cloud and a super cavitations that a cloud cavitation occurs at the smaller dynamic pressure $4\text{Pa} < \rho u_{in}^2/2 < 17\text{Pa}$, and a super cavitation is observed at the larger dynamic pressure $21\text{Pa} < \rho u_{in}^2/2 < 78\text{Pa}$. Thus, cavitation patterns map can be made on the chart degree of subcool with the dynamic pressure by data for a wide range of Reynolds numbers $0.24 \times 10^6 < Re < 2.3 \times 10^6$ at a fix angle of attack.

On the map, let us put a vertical line at a certain dynamic pressure, and trace the line from the bottom to the top, then it goes though some cavitation region with the increase of cavitation number. Meanwhile, on Le's map, put a vertical line at a certain angle of attack, and trace the line, then it also goes though some cavitation region with the increase of cavitation number. Actually, the former line corresponds to the latter line for the equivalent condition. It suggests that a three dimensional cavitation patterns map is available, which has three axes, angle of attack, dynamic pressure, and degree of subcool.

Second, let us focus on nitrogen results on $L_C = 60$ mm hydrofoil in $W = 60$ mm channel at $AOA = 8^\circ$ as shown at the right in Fig. 8. The same tendencies as observed for the water results can be seen. A shear and a partial cavitation regions are distinguished by cavitation number, however, a cloud and a super cavitations coexist in the region of $0.4 < \sigma < 1.8$. For example, in the region of $0.5 < \sigma < 1.0$, a cloud cavitation occurs at the smaller dynamic pressure $34\text{Pa} < \rho u_{in}^2/2 < 48\text{Pa}$, and a super cavitation is observed at the larger dynamic pressure $51\text{Pa} < \rho u_{in}^2/2 < 73\text{Pa}$. The map also can be made in nitrogen case.



$L_C = 60$ mm $W = 30$ mm Water $AOA = +8^\circ$



$L_C = 60$ mm $W = 60$ mm Liquid nitrogen $AOA = +8^\circ$

Fig.8 Cavitation patterns on charts of Degree of subcool and Dynamic pressure

5. STEADY AND UNSTEADY CAVITATIONS

A partial cavitation, a shear cavitation, and a super cavitation were almost steady except there are some small perturbations in cavity length and thickness. Only a cloud cavitation involves a large scale collapse of the cavity on the hydrofoil as shown in Figs. 6, 7. Here the cavity is strictly defined as the first seamless volume consisting of cavitation on the hydrofoil. For example, in case of $AOA = -4^\circ$, relationship of cavity length with Reynolds number are shown in Fig. 9. The left chart shows in the case of unsteady cavitation, and the right one shows in the case of steady cavitation. In these figures, each symbol denotes the minimum cavity length, and the upper end denotes the maximum cavity length because there are some perturbations even in the cases of steady cavitation.

For an unsteady cavitation, all of symbols are pointed below unity. It means that the end of the cavity stays on the hydrofoil for a moment at least per every departure. Moreover, almost the upper ends exist above 0.6. Wade & Acosta (1966) [1] experimentally found that a cavity is unsteady over a region of approximately $0.6 \leq L / L_C \leq 1.2$ regardless of angle of attack. Wu (1956) [19] theoretically induced that a solution shows the singularity behavior when a cavity length is comparable to the chord length $L / L_C \approx 1$ by improving Tulin's free stream analysis (1955) for super cavitation. Namely, a cavity is unsteady at near $L / L_C \approx 1$. Acosta (1955) [20] theoretically derived that a cavity is unsteady in a region of $0.74 < L / L_C$ by improving Tulin's free stream analysis for a partial cavitation. According to their results, in cases that the end section of the cavity enters the unstable region (a gray region of $0.6 \leq L / L_C \leq 1.2$ in the figures as stated by Wade & Acosta), the part of the cavity is torn from the hydrofoil and departs as a cloud cavitation. A cloud cavitation is triggered by an adverse pressure gradient on the hydrofoil as mentioned by Callenaere (2001) [3],

i.e. the gray unstable region corresponds the adverse pressure gradient region. In fact, as shown in Fig. 10, a flow near the outer edge of the cavity goes downward, however, a flow near the hydrofoil surface in the cavity is almost still or goes upward due to the adverse pressure gradient. Therefore, in this region, cavitation is rotated because of relative velocity difference, then the rear part of the cavity is torn from the hydrofoil surface. This is a mechanism of the unstable region in a range of $0.6 \leq L / L_C \leq 1.2$.

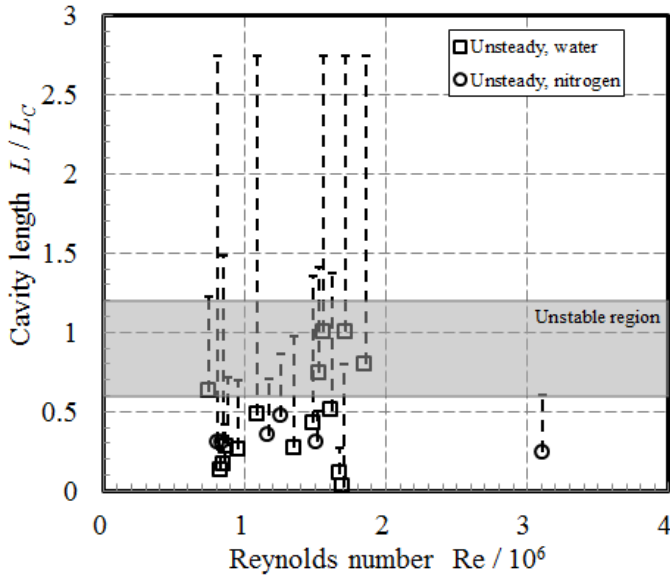
6. CONCLUSION

Cavitation around a plano-convex hydrofoil in a channel flow with various angle of attack -8° to $+8^\circ$, various Reynolds number 0.24×10^6 to 2.3×10^6 , and various cavitation number -1.1 to 85.1 was observed by a blow-down type cavitation tunnel with flow visualization. Liquid nitrogen and hot water were employed as working fluids. The experimental results are summarized as follows;

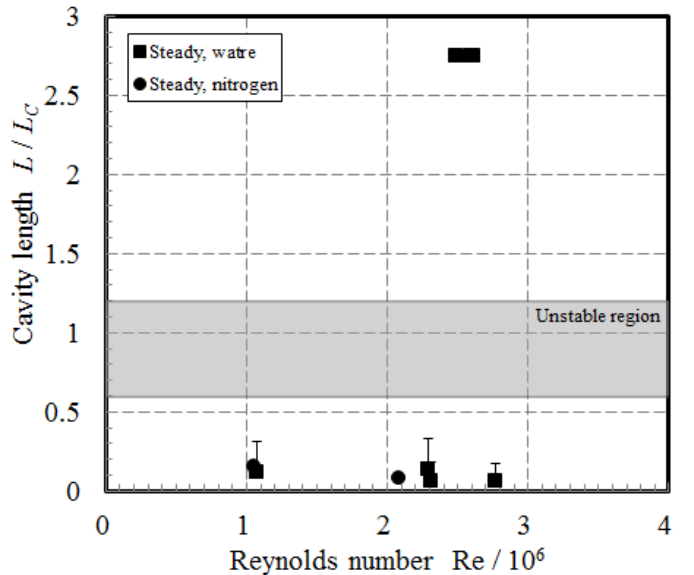
- 1: Cavitation patterns can be sorted into a partial cavitation, a shear cavitation, a cloud cavitation, and super cavitation in the same way as Le's water free surface flow although our experiments were done in liquid nitrogen and water channel flows.
- 2: For a certain fixed angle of attack and a certain fixed hydrofoil chord length, cavitation patterns map can be made on the chart of degree of subcool with dynamic pressure when data have a wide range of Reynolds number.
- 3: Only a cloud cavitation is unsteady cavitation with a large scale decay of the part of the cavitation. Even though the part of the cavity exist in a range of $0.6 \leq L / L_C \leq 1.2$ for a moment at least, the cavity is unsteady and a cloud cavitation occurs.

ACKNOWLEDGMENTS

This work was supported by KAKENHI (14750720) and the Iwatani Naoji Foundation.

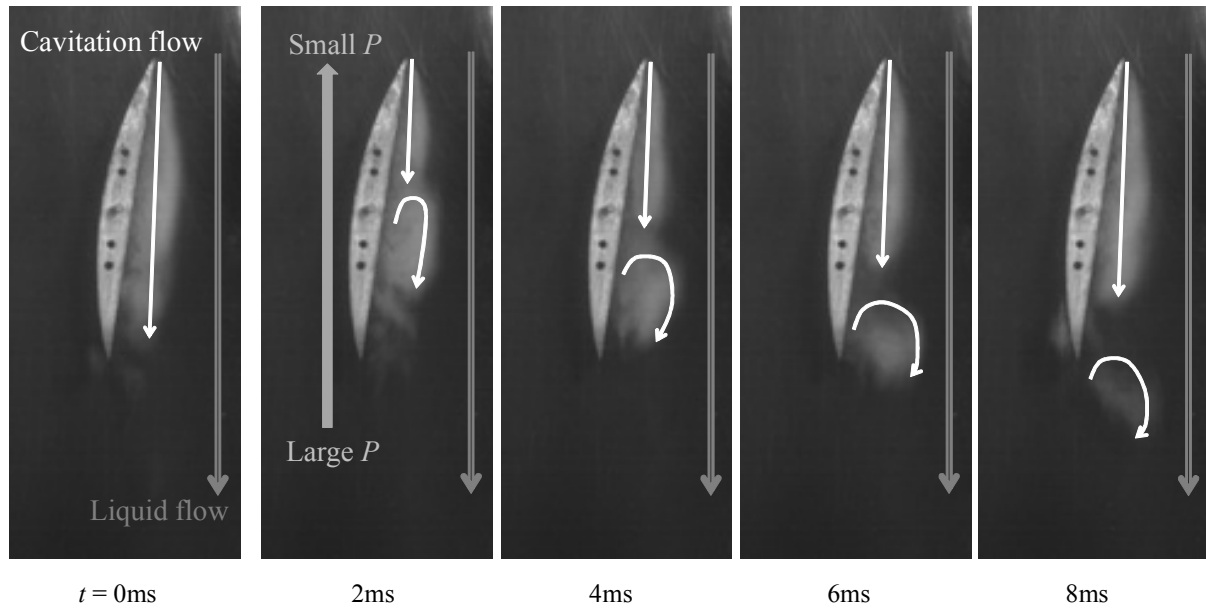


Unsteady cavitation (a cloud cavitation)



Steady cavitation (a partial, a shear, and a super cavitations)

Fig.9 Cavitation length versus Reynolds number in the cases of unsteady and steady cavitation at $AOA = -4^\circ$



$t = 0\text{ms}$

2ms

4ms

6ms

8ms

LN_2 $\text{AOA} = -8^\circ$ $T_{in} = -196.36^\circ\text{C}$ $\text{Re} = 3.29 \times 10^6$ $\sigma = 0.637$ $L_C = 60\text{mm}$ $W = 60\text{mm}$ (Y283)

Fig.10 Cloud cavitation shedding procedure at $\text{AOA} = -8^\circ$

REFERENCES

1. Wade, R. B. and Acosta A. J. 1966, "Experimental observation on the flow past a plano-con- vex hydrofoil", *Trans. ASME, J. of Basic Engineering*, 88, pp. 273-283
2. Le, Q., Franc, J. P. and Michel, J. M. 1993, "Partial cavities: Global behaviour and mean pressure distribution", *Trans. ASME, J. of Fluid Engineering*, 115, pp. 243-248
3. Callenaere, M., Franc, J. P., Michel, J. M., Riondet, M. 2001, "The cavitation instability by the development of a re-entrant jet", *J. of Fluid Mechanics*, 444, pp. 223-256
4. Stahl, H. A., Stepanoff, A. J., and Phillipsburg, N. J. 1956 "Thermodynamic aspects of cavitation in centrifugal pumps", *Trans. ASME*, 78, pp. 1691-1693
5. Salemann, V. 1959, "Cavitation and NPSH requirements of various liquids", *Trans. ASME, J. of Basic Engineering*, 81, pp. 167-180
6. Stepanoff, A. J. 1961, "Cavitation in centrifugal pumps with liquids other than water", *Trans. ASME, J. of Engineering for Power*, 83, pp. 79-90
7. Spraker, W. A. 1965, "The effects of fluid properties on cavitation in centrifugal pumps", *Trans. ASME, J. of Engineering for Power*, 87, pp. 309-318
8. Meng, P. R. 1968, "Change in inducer net positive suction head requirement with flow coefficient in low temperature hydrogen (27.9° to 36.6°R)", *NASA TN D-4423*
9. Hord, J. 1973 "Cavitation in Liquid Cryogenics II – Hydrofoil", *NASA CR-2156*
10. Simoneau, R. J., Hendricks, R. C 1979, "Two-phase choked flow of cryogenic fluids in converging-diverging nozzle", *NASA TP-1484*
11. Ludtk, P. R., Daney, D. E 1988, "Cavitation characteristics of a small centrifugal pump in He I and He II", *Cryogenics*, 28, pp. 96-100
12. Walstrom, P. L., Weisend II, J. G, Maddocks, J. R., Van Sciver, S. W. 1988, "Turbulent flow pressure drop in various He II transfer system components", *Cryogenics*, 28, pp. 101-109
13. Daney, D. E. 1988, "Cavitation in flowing superfluid helium", *Cryogenics*, 28, pp. 132-136
14. Pettersen, M. S., Naud, C., Baliba, S., Maris, H. J. 1994, "Experimental observations of cavitation in superfluid helium-4", *Physica B*, 194-196, pp. 575-576
15. Hori, S., Ito, Y., Yamaguchi, K. 2000, "Observation of Cavitation Bubbles in Cryogenic 2D Nozzle Flows", *Proc. of 40th Aerospace Propulsion Conference*, pp. 169-174, in Japanese
16. Ishii, T., Murakami, M 2003, "Comparison of cavitating flows in He I and He II", *Cryogenics*, 43, pp. 507-514
17. Ito, Y., Sawasaki, K., Tani, N., Nagasaki, T., Nagashima, T. 2005, "A Blowdown Cryogenic Cavitation Tunnel and CFD Treatment for Flow Visualization around a Foil", *Journal of Thermal Science*, 14, No.4, pp. 346-351
18. Ito, Y., Seto, K., N., Nagasaki, T. 2009, "Periodical shedding of cloud cavitation from a single hydrofoil in high-speed cryogenic channel flow", *Journal of Thermal Science*, 18, No. 1, pp. 58-64
19. Wu, T. Y. 1956, "A note on the linear and nonlinear theories for fully cavitated hydrofoil", *California Institute of Technology Report No. 21-22*
20. Acost A. J., 1955, "A note on partial cavitation of flat plate hydrofoil", *California Institute of Technology Report No. E19-19*

Experimental Analysis of Cavitating Behavior around a Clark Y Hydrofoil

Satoshi Watanabe*

Department of Mechanical Engineering
Kyushu University
Japan

Issei Nakamura

Graduate School of Engineering
Kyushu University
Japan

Yusuke Konishi

Graduate School of Engineering
Kyushu University
Japan

Akinori Furukawa

Department of Mechanical Engineering
Kyushu University
Japan

E-mail: fmnabe@mech.kyushu-u.ac.jp

ABSTRACT

Unsteady cavitating flow and hydraulic performance of a Clark-Y 11.7% hydrofoil were studied in order to clarify the relationship between the performance breakdown mechanism due to cavitation and the unsteady cavity behavior. Time-averaged pressure distributions around the hydrofoil were measured through pressure tap holes on the surface of the hydrofoil in several cavitation numbers with the angle of attack of 8.0 and 2.0 degrees. Then, lift coefficients were estimated by integrating the measured pressure distributions. In addition, the cavitating flow was filmed from the top and the side simultaneously using two high speed video cameras, and the unsteady static pressures just upstream and downstream of the hydrofoil were also simultaneously measured with the high speed video camera recording.

It is confirmed that, as the cavitation number is decreased, the estimated lift slightly increases from that in the non-cavitating condition just before the sudden breakdown, which has been reported by the past literatures. This tendency is more apparent in the angle of attack of 8 degrees. In this cavitation number region, the sheet cavity length largely oscillates, which is often called "partial cavity oscillation" due to the formation of large cloud cavity from the rear part of sheet cavity, being shed downstream. During the sudden breakdown, the cavity oscillates violently from super cavitation to cavitation-free states with low frequency, which is called "transitional cavity oscillation." The cloud cavity shedding is also observed, but is independent from the phase of transitional cavity oscillation.

NOMENCLATURE

B: Span of hydrofoil
C: Chord length of hydrofoil
C_L: Lift coefficient
C_p: Pressure coefficient around hydrofoil, $=2(p - p_{ref})/\rho U^2$
f: Frequency
l: Sheet cavity length
p: Pressure
p_{up}, *p_{down}*: Upstream and downstream pressure
p_{ref}: Reference pressure
p_v: Vapor pressure

St: Strouhal number, $=fC/U$

U: Main flow velocity

x: Coordinate along the chord

α : Angle of attack

ρ : Density

σ : Cavitation number, $=2(p_{ref} - p_v)/\rho U^2$

1. INTRODUCTION

Cavitation is an unavoidable phenomenon for high speed turbopumps, especially for inducers. Cavitation instabilities such as rotating cavitation and cavitation surge are major concern in the development of modern turbopump inducers for rocket engines. And also, even in the simple case of isolated two-dimensional hydrofoil, it is well known that the attached cavity developing on the suction surface becomes unstable and causes a strong vibration when the cavity length exceeds about 75% of the chord length (Wade and Acosta [1], Kawanami et al. [2], and etc.). This type of oscillation is called "transitional cavity oscillation," under which the cavity dramatically changes between partial and super cavities with low frequency. There is another cavitation instability, called "partial cavity oscillation," which has been recognized through careful visual observation and unsteady pressure measurements by several researchers (Le et al. [3], Arndt et al. [4] and Sato et al. [5]). Under this oscillation, it is often observed that the cloud cavities are periodically shed from the cavity trailing edge. The frequency of this oscillation decreases as the cavity becomes longer, keeping the Strouhal number based on the cavity length almost constant. The cavitation instabilities of two-dimensional hydrofoil seem to be classified mainly into above two oscillations. Their frequency characteristics have been well simulated by theoretical analysis (Watanabe et al. [6]).

The recent rapid progress of computer science including hardware technology as well as numerical simulation technology has enabled us to simulate the cavitating flow and achieve the qualitative, and in some extent, the quantitative agreements with real flow from basic ones such as cavitating hydrofoils and high-speed projectiles to practical ones such as cavitating pumps and hydroturbines. However, such cavitation CFD (Computational

Fluid Dynamics) still often fails to predict the cavitation performance in some cases. Recently, in order to clarify the intrinsic limitation of existing cavitation models and CFD codes with them, Turbomachinery Society of Japan has organized an industry-university collaborative research project on cavitation CFD (Project leader, Prof. C. Kato of The University of Tokyo.) Under this project, benchmark tests using four major commercial CFD solvers as well as four in-house or open source CFD solvers, equipped with various cavitation models, have been done for the cavitating flow around two types of hydrofoils, NACA0015 and Clark Y 11.7% (see Kato [7]), and it has been shown that none of the cavitation models can correctly predict the sudden breakdown of the lift coefficient as observed in experiments, partially due to the under-prediction of the cavity length. Frikha et al [8] has also investigated the influence of cavitation model on the unsteady cloud cavitation around two-dimensional hydrofoils, and the similar results are observed for all the models tested. They claim that the single phase turbulence models are too diffusive especially for water-vapor two-phase flow regions, and the modification of the turbulence viscosity is necessary to well simulate the cloud cavitation phenomenon. On the other hand, Wosnik et al. [9] has reproduced the vortical flow structures with cloud cavitation by their two-dimensional large eddy simulation with simple barotropic cavitation model.

For the development of more reliable cavitation CFD solvers, which can quantitatively predict the hydraulic performance degradation of hydromachinery along with the development of cavitation, it is necessary to provide the sufficient data on the unsteady cavitating flow structures and its relation to the performance breakdown mechanism. For this purpose, unsteady cavitating flow and hydraulic performance of a Clark-Y 11.7% hydrofoil were studied in the present study. Time-averaged pressure distributions around the hydrofoil were measured through pressure tap holes on the surface of the hydrofoil in several cavitation numbers with the angle of attack of 8.0 and 2.0 degrees. Then, lift coefficients were estimated by integrating the measured pressure distributions. In addition, the cavitating flow was filmed from the top and the side simultaneously using two high speed video cameras, and the unsteady static pressures just upstream and downstream of the hydrofoil were also simultaneously measured with the high speed video camera recording.

2. EXPERIMENTAL APPARATUS

Present experiments have been done using a cavitation tunnel in Kyushu University (Watanabe et al. [10]). This tunnel has a rectangular test section with the width (height) of 200mm and the span of 81.5mm. The top, bottom and one of side walls of the test section consist of a transparent acrylic resin for visual observations. Test obstacles can be set horizontally at the center on another side wall with arbitrary angle of attack. In the present study, a two-dimensional Clark Y 11.7% hydrofoil with the chord length of $C=100$ mm and the span of $B=81.0$ mm as shown in Fig. 1 is tested. The tunnel height to the chord length ratio is $200 \text{ mm}/100 \text{ mm} = 2.0$, indicating a substantial blockage effect of tunnel walls, which will be described later.

The following two series of measurements are done with the main velocity of $U=8.3 \text{ m/s}$ (then the Reynolds number based on

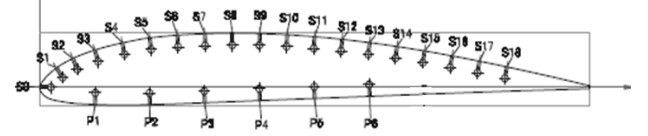


Fig. 1 Clark Y 11.7% hydrofoil

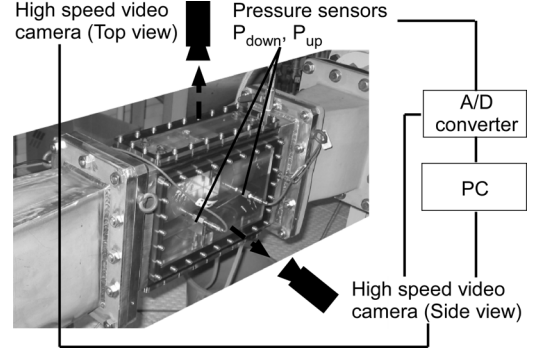


Fig.2 Setup for unsteady cavity observations

the chord length is 8.3×10^5) and the attack angle of $\alpha=2$ and 8 degrees; $\alpha=2$ degrees gives a good drag to lift ratio with moderate loading, and $\alpha=8$ degrees gives a large lift force.

Pressure distribution measurements

In order to measure the pressure distribution around the hydrofoil, the model used is fitted with totally 25 pressure tap holes (1 at the leading edge, 18 and 6 respectively on the suction and pressure surfaces), as shown in Fig. 1. The locations of taps are, on the suction surface, 3, 6, 10, 15, 20, 25, 30, 35, 40, 45, 50, 55, 60, 65, 70, 75, 80 and 85% of chord length from the leading edge, while 10, 20, 30, 40, 50 and 60% on the pressure surface. The hole sizes are 0.5 mm for all the taps, which are connected through transparent polyurethane tube and hand-operated scanning valves to the piezo-resistive absolute pressure transducers (GE Measurement & Control Solutions, UNIK5000). The accuracy of the transducer itself is 0.2 kPa, and the overall error estimation is at most 1kPa taking account of the observed resolved gas column in the polyurethane tube. To obtain reliable time-averaged static pressures, we wait for more than a few minutes after operating the scanning valves, and then the measurements are done for 120 seconds with sampling frequency of 100 Hz. Then, the time-averaged data are used to calculate the pressure coefficient distribution $C_p(x)$ defined as follows.

$$C_p(x) = \frac{p(x) - p_{ref}}{\rho U^2 / 2} \quad (1)$$

where $p(x)$ and p_{ref} are pressure on the hydrofoil surface and at the reference location (200 mm upstream from the mid-chord), ρ the density of water, and U the velocity of main flow.

Unsteady cavity behavior observations

In order to understand the unsteady cavity behavior around the hydrofoil, high-speed video camera observations are carried out. Since the pressure tap holes stimulate more or less the occurrence of cavitation, a bare hydrofoil is used for this purpose. The cavitating flows are filmed from the top and the

side simultaneously using two high-speed video cameras (Vision Research, Phantom V310 and V4.3), as shown in Fig. 2. The frame rate is set to be 8,000 frame/s, and the spatial resolution was 704*256 and 512*128 pixels respectively for the top and the side views, covering the region between the leading edge of hydrofoil to about one-chord downstream of hydrofoil. The unsteady wall pressures about $0.2C$ upstream and downstream of hydrofoil, p_{up} and p_{down} , are measured, being synchronized with the each frame in the high speed video camera recording. Strain gage type pressure transducers (Kyowa Electronic Instruments, PGM-C-A-200KP) with the capacity of 200 kPa and resonance frequency of 24 kHz are employed and installed through the adapter filled with silicon oil, resulting in the decrease of the resonance frequency to several kHz.

In the experiments, the system pressure, the one in the upstream tank, is reduced step by step from the non-cavitating condition to the sufficiently low pressure condition with stable super-cavitation, and all the above measurements are done at the every system pressure. The amount of dissolved oxygen is checked to be less than 2 ppm before and after the experiments.

3. RESULTS AND DISCUSSIONS

Pressure distribution around hydrofoil

Figures 3 (a) and (b) show the measured pressure coefficient (C_p) distributions in various cavitation numbers σ from non-cavitating to super-cavitating conditions for $\alpha=8.0$ and 2.0 degrees, respectively. The cavitation number σ is defined as follows.

$$\sigma = \frac{p_{ref} - p_v}{\rho U^2 / 2} \quad (2)$$

where p_v denotes the vapor pressure.

The angle of attack of $\alpha=8.0$ degrees gives the large lift force. We can see a strong suction peak near the leading edge in the non-cavitation condition of $\sigma=3.01$, indicating that the cavity initiates near this location resulting in generally-called leading edge cavitation. At $\sigma=1.92$, we observe, in the high-speed camera observations, the short partial cavity with its leading edge showing the fingering pattern. We can see the flat distribution of pressure coefficient C_p with the value of about -1.9 near the leading edge on the suction side. When the pressure tap is covered by the vapor-filled cavity, the pressure there is approximately equal to the vapor pressure p_v . Therefore, the pressure coefficient C_p yields to be

$$C_p = \frac{p_v - p_{ref}}{\rho U^2 / 2} = -\sigma$$

Then, this flat C_p distribution with $C_p = -\sigma$ indicates that this area is cavitating region. Lower the cavitation number is, the region of the flat C_p distribution on the suction side becomes wider, indicating the development of cavitation. At $\sigma=1.44$, the location of the leading edge of the cavity becomes uniform, and the unsteadiness of cavity becomes remarkable due to the formation of large scale cloud cavity from the trailing edge of the cavity, as shown later. At σ less than 1.28, substantial cavity volume oscillation becomes predominant, inducing large pressure fluctuations upstream and downstream of the hydrofoil.

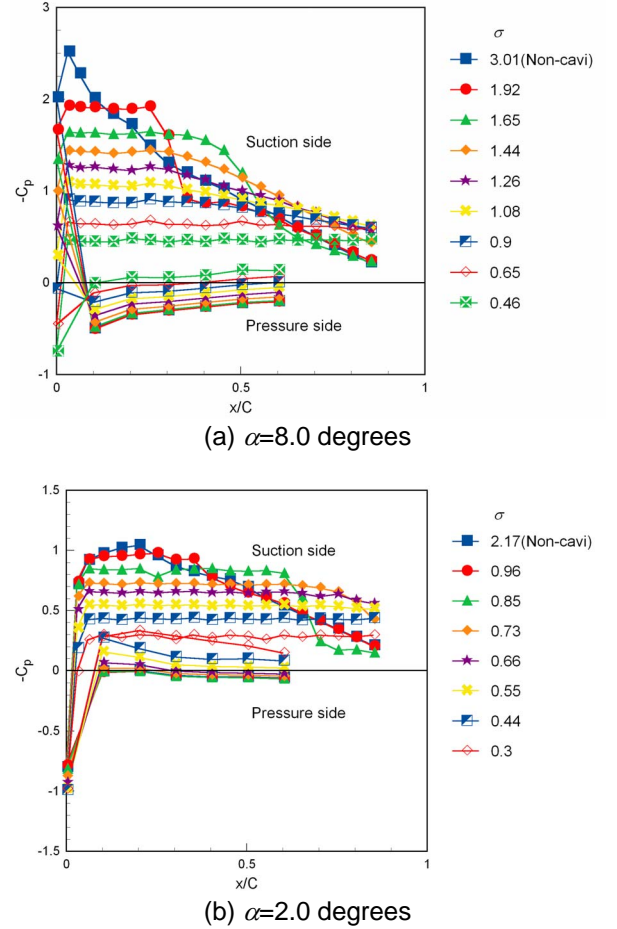


Fig. 3 Pressure coefficient distribution around Clark Y 11.7% hydrofoil for various cavitation numbers

Finally at $\sigma=0.46$, the cavity is already stable super-cavitation, and no significant pressure fluctuations can be observed.

On the other hand, for the angle of attack of $\alpha=2.0$ degrees, we can confirm a relatively flat pressure distribution and a weak suction peak around $x=0.2C$ in the non-cavitating condition of $\sigma=2.17$. At $\sigma=0.96$, we can see a flat C_p distribution round $x/C=0.06$ to 0.2 . However, the cavity does not cover over the all span of hydrofoil but only around the pressure tap holes, meaning that the existence of pressure taps more or less affects the appearance of cavitation as well as the pressure distribution. As the cavitation number is reduced, the flat C_p region becomes wider, indicating the development of cavitation.

For both cases with the angle of attack of $\alpha=8.0$ and 2.0 degrees, static pressures on the pressure side decrease with the decrease of cavitation number, i.e. the development of cavitation. The developed cavity on the suction side of hydrofoil imposes the blockage effect in a flow channel between the tunnel wall and the suction side of hydrofoil, and then the velocity along the pressure side increases, resulting in the decrease of the static pressure on the pressure side. This effect is remarkable in this study, since the channel height of the tunnel to the hydrofoil chord ratio is small as 2.0. It is important to take account of the geometry of test section when CFD simulation is carried out.

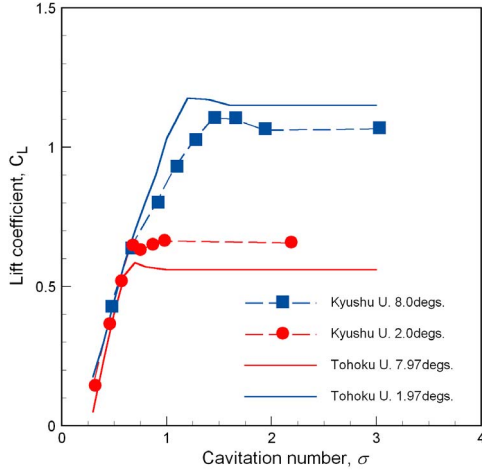


Fig. 4 Estimated lift coefficient compared with direct measurement by Numachi [11]

Next, by integrating the C_p distribution along the hydrofoil surface, we can estimate the pressure forces as follows.

$$\frac{\mathbf{F}_p}{\rho U^2 BC/2} = (C_D, C_L) = \frac{1}{C} \oint C_p \mathbf{n} ds \quad (3)$$

where \mathbf{F}_p denotes the pressure force, and C_D and C_L the drag and lift coefficients due to the pressure force. Numerical integration has been done with the linear interpolation of the pressure coefficient C_p shown in Fig. 3, and the evolution of C_L against the decrease of cavitation number σ is plotted in Fig. 4. In this figure, the lift coefficient directly measured by the force balance by Numachi [11] is also plotted by solid lines. The tunnel height to chord length ratio is 190 mm/70 mm = 2.71 in Numachi's experiments, which is larger than 2.0 of the present experiments. Then, the blockage effect is expected to be more significant in the present study.

By comparing the present results with the Numachi's experiments, we can see the qualitative agreement; as the cavitation number is decreased, the estimated lift slightly increases from that in the non-cavitating condition just before the sudden breakdown. The present study underestimates the lift coefficient for the angle of attack of $\alpha=8$ degrees, but overestimates for $\alpha=2$ degrees. For $\alpha=8$ degrees, the stagnation point near the leading edge locates on the pressure side, but it cannot be recognized in the pressure distribution shown in Fig. 3, due to the sparse measurement points, which results in the underestimation of the lift coefficient for $\alpha=8$ degrees.

The breakdown cavitation number is larger in the present study, and this is more remarkable for the angle of attack of $\alpha=8$ degrees. This is due to the stronger blockage effect in the present study.

Unsteadiness of sheet cavity

Figure 5 summarizes the time-averaged sheet cavity length and its fluctuation range plotted against the cavitation number σ for the angle of attack of $\alpha=8.0$ degrees. The cavity length is measured every 20 frames of totally 8,000 frames in one second from high-speed camera observations. In order to examine the effect of the existence of pressure tap holes on cavitating flow behaviors, we measure the cavity length for both the hydrofoil

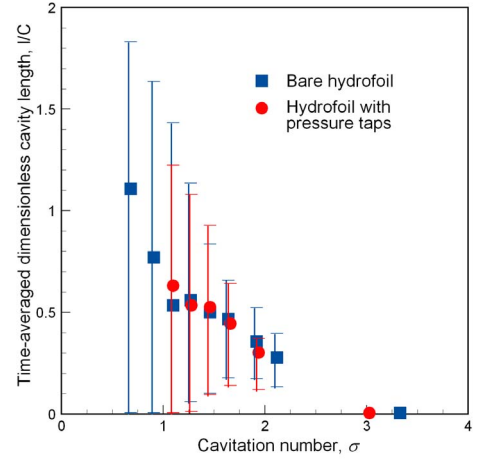


Fig. 5 Averaged sheet cavity length and range of cavity length fluctuation for $\alpha=8.0$ degrees

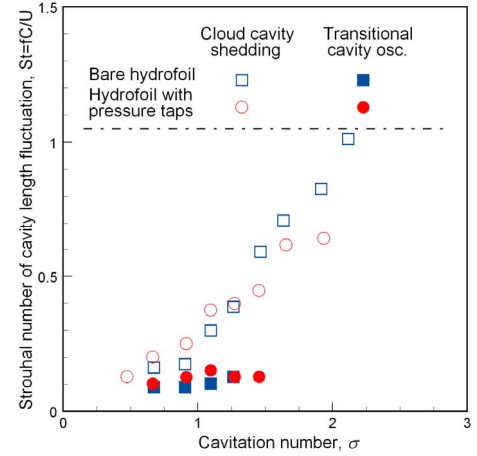


Fig. 6 Strouhal number of cavity length fluctuations for $\alpha=8.0$ degrees

model with pressure tap holes and the bare hydrofoil model. As a result, there is a fairly good agreement between two models, indicating that the overall cavity behaviors are not altered by the existence of pressure tap holes, although they seem to affect the cavity near the leading edge.

Figure 6 shows the Strouhal numbers of sheet cavity length fluctuation, based on the chord length, for the angle of attack of $\alpha=8.0$ degrees. Both the results with the hydrofoil model with pressure tap holes and the bare hydrofoil model are plotted in the figure, and they agree fairly well with each other.

There are two main components; For larger cavitation numbers of $\sigma > 1.3$, which corresponds to the time-averaged cavity length less than 50% chord and the maximum length less than 100% chord as shown in Fig. 5, only the higher frequency component is observed and the frequency decreases with the decrease of σ , which is similar to so-called "partial cavity oscillation" (Watanabe et al., [6]). Through the high speed video camera observation, the elongation of the sheet cavity followed by the formation of the cloud cavity from the trailing edge of sheet cavity which shortens the sheet cavity is confirmed. The

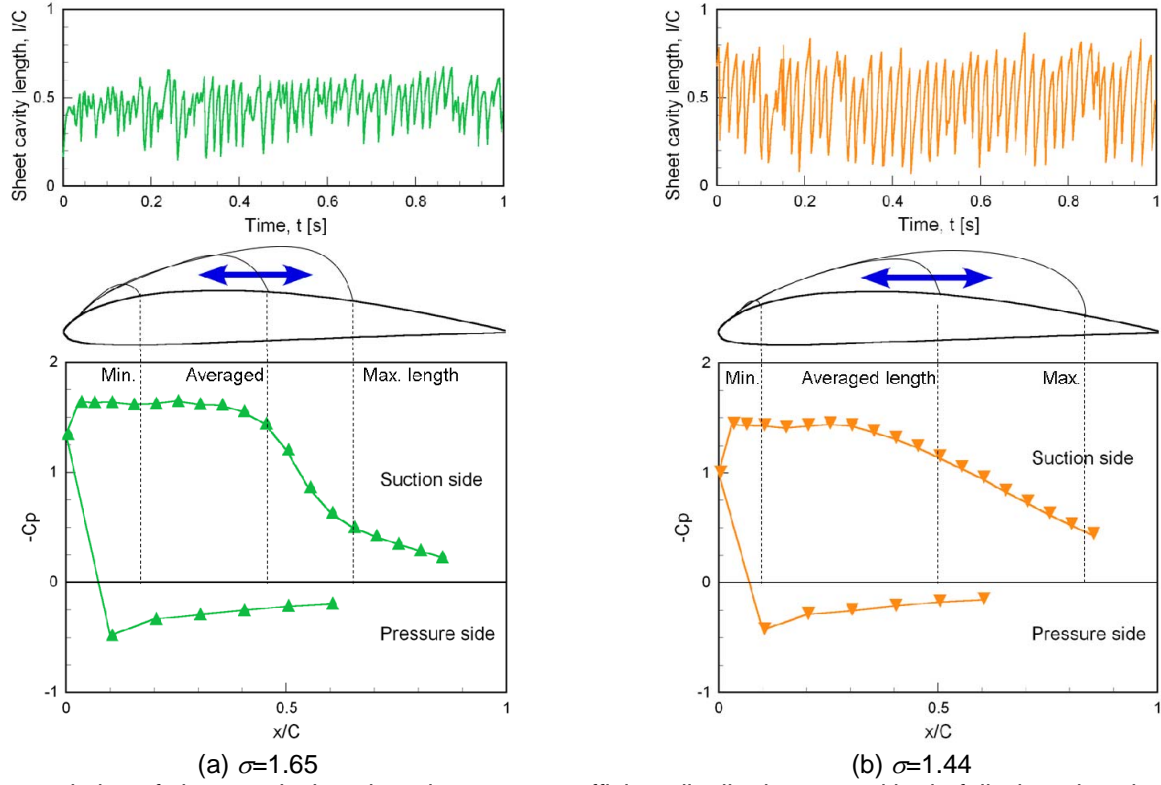


Fig. 7 Time evolution of sheet cavity length and pressure coefficient distribution around hydrofoil where location of trailing edge of sheet cavity with its averaged, maximum and minimum length are indicated ($\alpha=8.0$ degrees)

cloud cavity shedding is the main cause of the partial cavity oscillation in the present study.

For smaller cavitation numbers of $\sigma < 1.3$, there is another low frequency component, that is so-called “transitional cavity oscillation”. During the one cycle of this low frequency component, the cavity significantly oscillates from cavitation-free state to super cavitation.

Partial cavity oscillation

Figures 7 (a) and (b) show the time evolution of the sheet cavity length and the time-averaged pressure coefficient (C_p) distribution around the hydrofoil for the cavitation number of $\sigma = 1.65$ and 1.44 respectively. A high frequency oscillation of sheet cavity length indicating the occurrence of partial cavity oscillation can be seen in both cases.

Figure 8 shows the typical example pictures of sheet cavity from top view during once cycle of partial cavity oscillation for $\sigma = 1.44$. At $t=0.400$ s, a short sheet cavity and a cloud cavity behind it can be observed. As time goes by, the sheet cavity is convected downstream and the sheet cavity grows gradually. Finally, another cloud cavity is formed from the trailing edge of sheet cavity and the sheet cavity is shortened at $t=0.425$ s. The partial cavity oscillation is maintained by this process, and the formation of the cloud cavity plays an important role in the partial cavity oscillation.

In the bottom figure showing the pressure coefficient (C_p) distribution around the hydrofoil in Figs. 7(a) and (b), the locations of trailing edge of sheet cavity with the time-averaged, maximum and minimum cavity length are indicated by broken lines. In the former region of sheet cavity (let's say $x/C < 0.3$), the

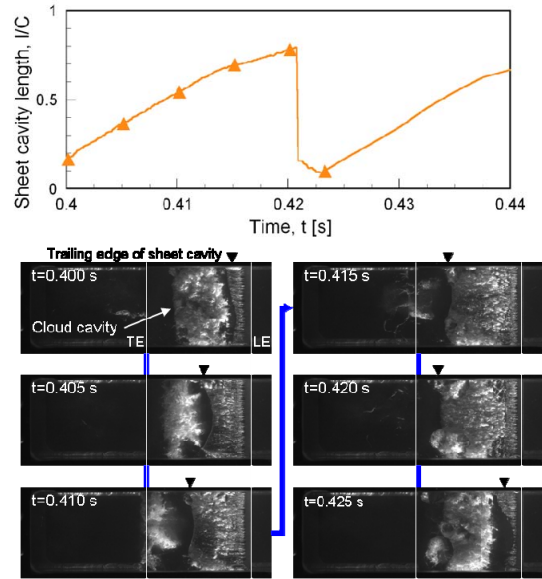


Fig. 8 Example pictures for once cycle of partial cavity oscillation ($\alpha=8.0$ degrees, $\sigma=1.44$)

pressure taps there are covered by the cavity during the most part of oscillation cycle, and the time-averaged pressure is almost equal to the vapor pressure ($C_p = -\sigma$). On the other hand, in the rear region of the sheet cavity, the pressure taps are exposed from the cavity during some part of the oscillation cycle, and then the pressure gradually increases in this region.

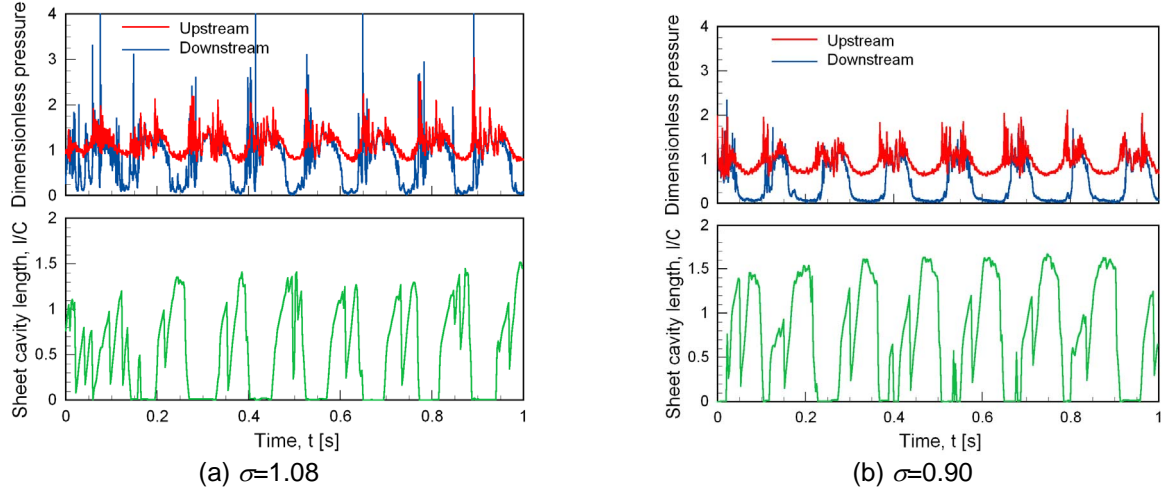


Fig. 9 Time evolutions of upstream and down stream pressures and sheet cavity length for $\alpha=8.0$ degrees

This tendency is more apparent for $\sigma=1.44$ due to the larger amplitude of cavity length fluctuation.

Recalling the cavitation performance of hydrofoil shown in Fig. 4, we can notice that the lift coefficient C_L at $\sigma=1.92$ is almost the same as that in the non-cavitating condition, whereas the slight increase in C_L can be seen at $\sigma=1.65$ and 1.44 . At $\sigma=1.92$, the fluctuation of sheet cavity is not very significant, and the pressure downstream of sheet cavity rapidly increases from the vapor pressure as shown by red closed circles in Fig. 3(b). On the other hand, at $\sigma=1.65$ and 1.44 , the fluctuation of sheet cavity length becomes significant, and the pressure recovery downstream of the sheet cavity is more gradual than that at $\sigma=1.92$, contributing the slight increase of C_L at $\sigma=1.65$ and 1.44 . This suggests that, in order to reproduce precisely the cavitation performance of hydrofoil by CFD, especially the slight increase of the lift coefficient just before the breakdown, the cavitation model has to be able to reproduce the unsteady behavior of sheet cavity associated with the formation of large scale cloud cavity. And/or, the appropriate boundary conditions considering the response of tunnel facility to cavitation might be necessary to realize it.

Transitional cavity oscillation

Figures 9 (a) and (b) show the time evolutions of pressures just upstream and downstream of hydrofoil and the sheet cavity length for (a) $\sigma=1.08$ and (b) $\sigma=0.90$, respectively. In both cases, the cavity changes drastically with low frequency (less than 10 Hz), indicating the occurrence of transitional cavity oscillation.

Figure 8 shows the typical example pictures of sheet cavity from top and side views during one cycle of transitional cavity oscillation for $\sigma = 1.08$. The sheet cavity elongates gradually from the partial to super cavitations during $t=0.57$ - 0.61 s. At $t=0.615$ s, the large cloud cavity is formed and the sheet cavity is suddenly shortened. After that the cloud cavity is convected downstream and the sheet cavity grows again. At around $t=0.630$ s the sheet cavity length takes the maximum value during this one cycle of transitional cavity oscillation, and then the sheet cavity begins to shrink with the small vortical cavities released from its trailing edge. Finally, all the cavity disappears at $t=0.660$ s.

It is interesting to see that, the number of formation of large-scale cloud cavity seems not to be fixed during one cycle of transitional cavity oscillation; for example, at $\sigma=0.90$, twice in one cycle but three times in another. This fact implies that the transitional cavity oscillation is independent of the formation of the cloud cavity. Since the frequency of transitional cavity oscillation is very low, the formation of cloud cavity can be done several times associated with the elongation of the sheet cavity.

As has been shown in Fig. 6, the transitional cavity oscillation occurs with the cavitation number σ less than approximately 1.30 for $\alpha=8.0$ degrees. From the lift coefficient shown in Fig. 4, we can find that the lift coefficient has begun to decrease at $\sigma=1.29$. This situation suggests that the transitional cavity oscillation occurs during the lift breakdown.

4. CONCLUSIONS

In the present study, the unsteady cavitating flow and hydraulic performance of a Clark-Y 11.7% hydrofoil were studied in order to clarify the relationship between the performance breakdown mechanism due to cavitation and the unsteady cavity behavior. For the hydraulic performance measurement, time-averaged pressure distributions around the hydrofoil were measured through pressure tap holes on the surface of the hydrofoil in several cavitating conditions. To understand the unsteady cavity behavior, the cavitating flow was filmed from the top and the side simultaneously using two high speed video cameras, and the unsteady static pressures just upstream and downstream of the hydrofoil were also simultaneously measured with the high speed video camera recording.

The lift coefficient estimated from the measured pressure distribution shows a slight increase at light cavitating conditions, which has been observed by direct measurements of lift force done in past literatures. At these conditions, the partial cavity oscillation with large amplitude is observed, which affects the pressure distribution in the rear fluctuating part of the cavity, resulting in the increase of the lift coefficient. The formation of the large scale cloud cavity from the rear part of the cavity is responsible for the partial cavity oscillation for large angle of attack.

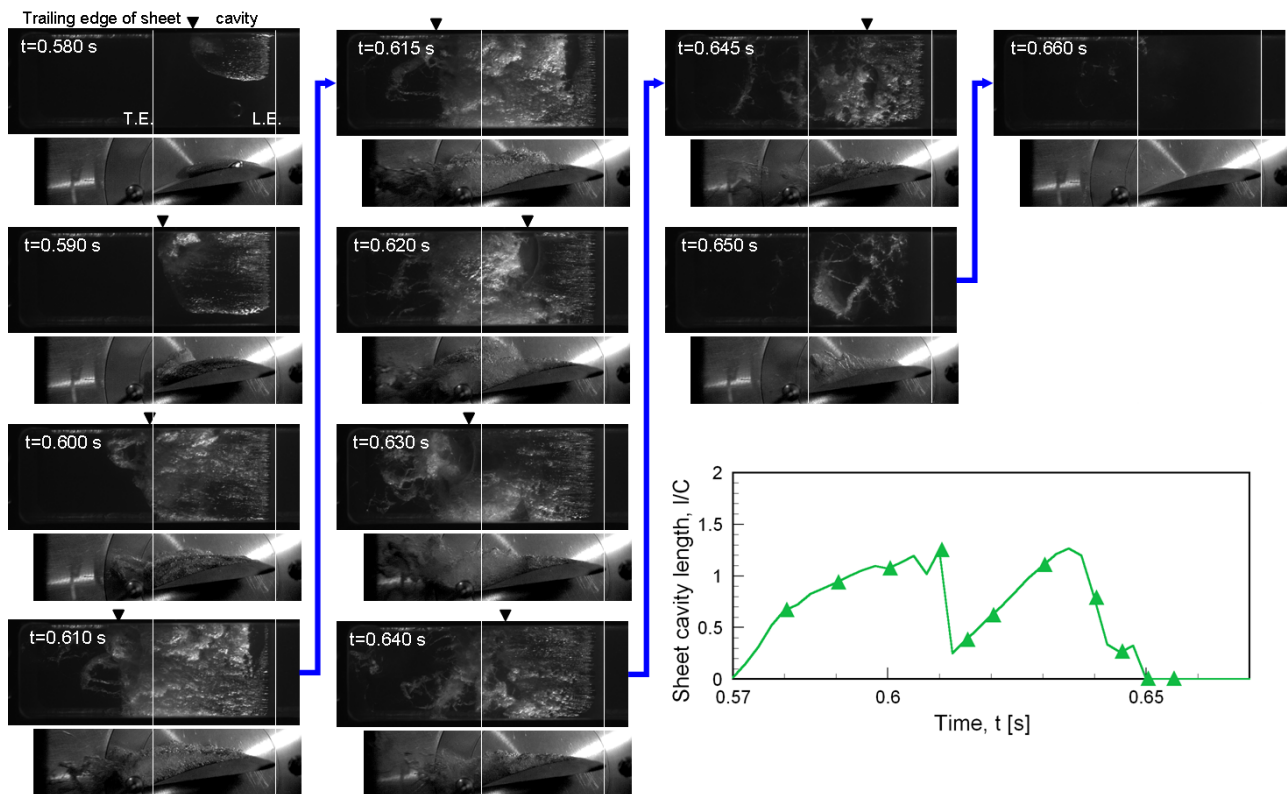


Fig. 10 Example pictures for once cycle of transitional cavity oscillation ($\alpha=8.0$ degrees, $\sigma=1.08$)

Further lowering the cavitation number, the lift coefficient begins to decrease, and another instability, transitional cavity oscillation, is observed. During one cycle of transitional cavity oscillation, the large scale cloud cavity is formed several times independently from the phase of the transitional oscillation.

ACKNOWLEDGMENTS

This study is partly supported by the JSPS Grant-in-Aid for Scientific Research (21686019). Some parts of this study are carried out under the industry-university collaborative research project on cavitation CFD (Project leader, Prof. C. Kato of The University of Tokyo) organized by Turbomachinery Society of Japan.

REFERENCES

- [1] Wade, R. B. and Acosta, A. J., 1966, "Experimental Observations on the Flow Past a Plano-Convex Hydrofoil," ASME J. Basic Eng., 88, pp. 273-283.
- [2] Kawanami, Y., Kato, H., Yamaguchi, H., Tanimura, M. and Tagaya, Y., 1997, "Mechanism and Control of Cloud Cavitation," ASME J. Fluids Eng. 119, pp. 788-794.
- [3] Le, Q. and Franc, J. P. and Michel, J. M., 1993, "Partial Cavities: Global and Mean Pressure Distribution," ASME J. Fluids Eng. 115, pp. 243-248.
- [4] Arndt, R. E. A., Song, C. C. S., Kjeldsen, M., He, J. and Keller, A., 2000, "Instability of Partial Cavitation: A Numerical/Experimental Approach," Proc. of 23rd Symp. on Naval Hydrodynamics, Val de Reuil.
- [5] Sato, K., Tanada, M., Monden, S. and Tsujimoto, Y., 2001, "Observations of Oscillating Cavitation on a Flat Plate

Hydrofoil," CAV2001: Fourth Int. Symp. on Cavitation, Pasadena, CA, USA, sessionB1.001.

- [6] Watanabe, S., Tsujimoto, Y. and Furukawa, A., 2001, "Theoretical Analysis of Transitional and Partial Cavity Instabilities," ASME J. Fluids Eng. 123, pp. 692-697.
- [7] Kato, C., 2011, "Industry-University Collaborative Project on Numerical Predictions of Cavitating Flows in Hydraulic Machinery – Part 1: Benchmark Test on Cavitating Hydrofoils -," Proc. ASME-JSME-KSME Joint Fluids Engineering Conference 2011, AJK2011-06084, to be presented.
- [8] Frikha, S., Coutier-Delgosha, O. and Astolfi, J. A., 2008, "Influence of the Cavitation Model on the Simulation of Cloud Cavitation on 2D Foil Section," Int. J. Rotating Machinery, Vol.2008, Article ID 146234.
- [9] Wosnik, M., Qin, Q., Kawakami, D. T. and Arndt, R. E. A., 2005, "Large Eddy Simulation (LES) and Time-Resolved Particle Image Velocimetry (TR-PIV) in the Wake of a Cavitating Hydrofoil," CD-ROM Proc. ASME 2009 Fluids Engineering Division Summer Meeting, Houston, Texas, FEDSM2005-77467.
- [10] Watanabe, S., Suefuji, T., Ikeda, A., Furukawa, A. and Nishii, K., 2009, "Experimental Study of Unsteady Cavitating Flow around a Flat Plate Hydrofoil with/without Tip Clearance," CD-ROM Proc. ASME 2009 Fluids Engineering Division Summer Meeting, Vail, Colorado, FEDSM2009-78506.
- [11] Numachi, F., 1938, "Cavitation Performance of 4 Types of Hydrofoil," (in Japanese), Trans. JSME, III, Vol.7, No. 28, pp. 1-9.

On the assessment of cavitation erosion on a hydrofoil using unsteady RANS

ZiruLi*/ Delft University of Technology, The Netherlands

Mathieu Pourquie/ Delft University of Technology, The Netherlands

Tom Van Terwisga/ Maritime Research Institute Netherlands (MARIN);
Delft University of Technology, The Netherlands

* Ziru.Li@tudelft.nl

ABSTRACT

Cavitation erosion is well-known to be one of the most annoying effects of cavitation on the ship propulsor and propulsor-aft ship configurations. This paper addresses the question whether the risk of cavitation erosion can be predicted by using contemporary unsteady RANS codes, without the necessity to compute the details of the actual collapse.

To investigate this question, a thorough study on the cavitation phenomena over a 2D NACA0015 hydrofoil with an angle of attack of 6 deg is investigated at first, in order to obtain a better understanding of the nature of cavitation dynamics. Two flow regimes are included: non-cavitating and unsteady cavitating condition. It is concluded that a realistic dynamic behavior of break-up is only obtained by an artificial reduction of the turbulent viscosity in the regions of higher vapor volume fraction. Another case, the 2D NACA0015 hydrofoil with a different angle of attack of 8 deg is also investigated to show the effect of the angle of attack on the shedding behavior. Finally, in addition to a qualitative analysis of the pressure fluctuations during the collapse of cavities, an attempt to quantitatively evaluate the risk of cavitation erosion by a post-processing erosion model is made on the 3D NACA0015 hydrofoil at the 8 deg angle of attack.

NOMENCLATURE

C_p	Pressure coefficient
$C_{p\infty}$	Pressure coefficient at infinity
$C_{p\min}$	Minimum pressure coefficient
P	Local mixture pressure
P_v	Vapor pressure
P_0	Initial pressure at undisturbed condition
P_a	Acoustic pressure in the far field
R_e	Evaporation of the vapor bubbles
R_c	Condensation of the vapor bubbles
R	Bubble radius
R_0	Initial bubble radius
A	Radius of bubble cloud
r	Radial coordinate from the center of the cloud

t	Time
t_0	Initial time excluding the start-up effect
t^*	Dimensionless time, $t^* = (t - t_0) / \Delta t$
u	Mixture velocity
U	Reference velocity
S	Surface tension
D	Length scale
Re	Reynolds number, $Re = \rho_l U R_0 / \mu_E$
We	Weber number, $We = \rho_l U^2 R_0 / S$
Δt	Time step size
Δt^*	Dimensionless time step size
σ	Cavitation Number
α	Vapor volume fraction
ρ_m	Mixture density
ρ_l	Liquid density
ρ_v	Vapor density
μ_m	Mixture viscosity
μ_t	Turbulent viscosity
μ_E	Effective viscosity
k	Turbulence kinetic energy
ω	Turbulence specific dissipation rate
n_b	Bubble number density
η	Bubble population per unit liquid volume

1. INTRODUCTION

It is essential to assess cavitation hindrance in an early design stage of propulsion systems and other hydraulic machinery due to its potentially serious adverse effects. Cavitation erosion is well-known to be one of the most annoying effects of cavitation on the ship propulsor and propulsor-aft ship configurations. It may cause severe material damage leading to increased costly maintenance, and deterioration in performance together with aggravated vibration and noise. This paper aims at a methodology for an assessment of the risk of cavitation erosion on a hydrofoil by using contemporary unsteady RANS codes. A thorough study on the cavitation phenomena over a 2D hydrofoil (NACA0015) is made in order to obtain a better

understanding of the unsteady nature of cavitation. Experimental results on a 2D hydrofoil in a cavitation tunnel are available for validation work with the 3D simulation results.

Though cavitation erosion has been extensively investigated in the last decades, the full and detailed mechanisms producing cavitation damage are still subject to debate, let alone the quantitative assessment of the risk of cavitation erosion. Despite the fact that serious attempts to derive criteria for such assessments based on experiments have been derived in a more formal way (European EROCAV project [1]), there are still serious debates whether a certain type of cavitation is erosive or not. This paper focuses on the question whether the risk of cavitation erosion can be predicted from unsteady RANS codes, without the necessity to compute the details of the actual collapse process. This would then justify a focus on modeling efforts of the large scale cavity dynamics only.

The capability of the RANS codes to predict the unsteady cavitation dynamics is initially explored through the simulations of the cavitating flow around the 2D hydrofoil. With the RANS code FLUENT, the break-up of the sheet cavity and also the periodic shedding of the cloud cavity at the trailing edge of the sheet can however only be predicted by an artificial reduction of the turbulence viscosity in the regions of higher vapor volume fraction [2]. It is noted that RANS codes such as Open Foam and ReFresco do not need this viscous correction at least for the 2D simulation cases. However, it is necessary for ReFresco to use this Reboud's modification for the simulation of the shedding behavior for the Delft Twist-11 Foil.

A detailed analysis of the 3D simulation results provides a comparison with the experimental results. The qualitative link between the pressure fluctuations and the unsteady cavitation dynamics has been validated. The high values of the pressure peaks during the collapse of the cavities are a first indicator of the aggressiveness of the cavitating flow over a hydrofoil. A second indicator is made in evaluating the macro-scale cavity dynamics through a post-processing model with regard to erosion. To this end, an energy based approach has been studied, using the model by Wang and Brennen [3], for a quantitative relation between the numerical results by the unsteady RANS code and the risk of cavitation erosion.

2. NUMERICAL MODELS

2.1 GOVERNING EQUATIONS

The governing equations for a two-phase flow are based on a single-fluid approach, regarding the mixture as one liquid. The flow field is solved for the mixture continuity and momentum equations,

$$\frac{\partial}{\partial t}(\rho_m) + \nabla \cdot (\rho_m \vec{u}) = 0 \quad (1)$$

$$\begin{aligned} \frac{\partial}{\partial t}(\rho_m \vec{v}) + \nabla \cdot (\rho_m \vec{u} \vec{u}) \\ = -\nabla p + \nabla \cdot [\mu_m (\nabla \vec{u} + \nabla \vec{u}^T)] + \rho_m \vec{g} + \vec{F} \end{aligned} \quad (2)$$

Here the relationship between the mixture density ρ_m and the vapor volume fraction α is defined as:

$$\rho_m = \alpha \rho_v + (1 - \alpha) \rho_l \quad (3)$$

The subscripts m , v and l represent mixture, vapor and liquid phase respectively.

2.2 TURBULENCE MODELING

The *SST* $k - \omega$ turbulence model developed by Menter [4] is adopted in this study, which is a blending between the $k - \omega$ model in the near-wall region and the $k - \epsilon$ model in the far field. The refinements of the $k - \omega$ model and a blending function can make this model behave properly in both the near-wall and far-field zones. To improve the cavity dynamics in the simulation, a modification of the turbulent viscosity, μ_t , is applied following the idea of Reboud et al [5].

$$\mu_t = f(\rho) C_\omega \frac{k}{\omega} \quad (4)$$

$$f(\rho) = \rho_v + \frac{(\rho_m - \rho_v)^n}{(\rho_l - \rho_v)^{n-1}}; \quad n \gg 1 \quad (5)$$

With a recommended exponent value $n = 10$, the turbulent viscosity in the region with higher vapor volume fraction is reduced to better simulate the re-entrant jet and shedding behavior.

2.3 CAVITATION MODELING

The cavitation model adopted here is developed by Schnerr & Sauer [5]. The transport equation for the vapor volume fraction has the general form:

$$\frac{\partial}{\partial t}(\alpha \rho_v) + \nabla \cdot (\alpha \rho_v \vec{u}) = R_e - R_c \quad (6)$$

Where the source term R_e and R_c are connected to the evaporation and condensation of the vapor bubbles respectively, accounting for the mass transfer between the vapor and liquid phases in cavitation. The source terms are derived from the Rayleigh-Plesset equation and are defined as:

$$R_e = \frac{\rho_v \rho_l}{\rho_m} \alpha (1 - \alpha) \frac{3}{R} \sqrt{\frac{2}{3} \frac{(P_v - P)}{\rho_l}}, \quad \text{when } P_v \geq P \quad (7)$$

$$R_c = \frac{\rho_v \rho_l}{\rho_m} \alpha (1 - \alpha) \frac{3}{R} \sqrt{\frac{2}{3} \frac{(P - P_v)}{\rho_l}}, \quad \text{when } P_v \leq P \quad (8)$$

The bubble radius can be related to the vapor volume fraction α and the bubble number density n_b as follows:

$$R = \left(\frac{\alpha}{1 - \alpha} \frac{3}{4\pi n_b} \right)^{\frac{1}{3}} \quad (9)$$

Where n_b is the only parameter to be provided as input for FLUENT with a default value of $1e + 13$.

2.4 BUBBLE CLOUD MODEL

The bubble cloud model is proposed by Wang and Brennen in order to simulate the nonlinear growth and collapse of a cloud cluster of bubbles. It uses the fully nonlinear continuum mixture equations coupled with the Rayleigh-Plesset equation for the interaction of the bubbles with the flow.

This model considers a spherical bubble cloud surrounded by an unbounded pure liquid as the study subject (see Fig.1), and it is hypothesized that the population of bubbles per unit

volume of liquid η is piecewise uniform initially and remains constant and piecewise uniform within the cloud.

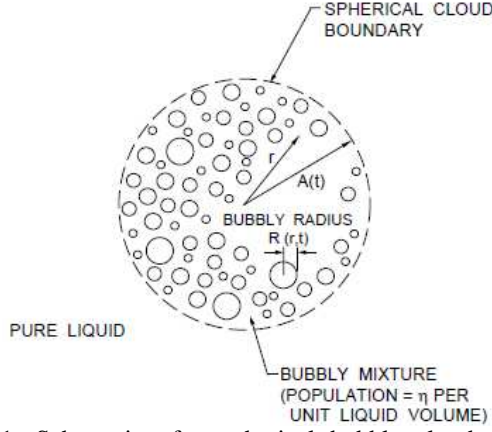


Figure 1: Schematic of a spherical bubble cloud (Wang & Brennen [3])

The dimensionless forms of the continuity and momentum equations for the spherical bubbly flow are:

$$\frac{1}{r^2} \frac{\partial(r^2 u)}{\partial r} = \frac{12\pi\eta R^2}{3 + 4\pi\eta R^3} \frac{DR}{Dt}; r \leq A(t) \quad (10)$$

$$\frac{Du}{Dt} = -\frac{1}{6}(3 + 4\pi\eta R^3) \frac{\partial C_p}{\partial r}; r \leq A(t) \quad (11)$$

and

$$\eta = \frac{\alpha / (1 - \alpha)}{\frac{4}{3} \pi R^3} \quad (12)$$

$$C_p(r, t) = \frac{P(r, t) - P_0}{\frac{1}{2} \rho_l U^2} \quad (13)$$

Where $P(r, t)$ is the mixture pressure and P_0 is the initial equilibrium pressure.

The dimensionless form of the Rayleigh-Plesset equation, which relates the local mixture pressure to the bubble dynamic, is:

$$R \frac{D^2 R}{Dt^2} + \frac{3}{2} \left(\frac{DR}{Dt} \right)^2 + \frac{4}{\text{Re}} \frac{1}{R} \frac{DR}{Dt} = \frac{\sigma}{2} (R^{-3\kappa} - 1) + \frac{2}{\text{We}} (R^{-3\kappa} - R^{-1}) - \frac{1}{2} C_p \quad (14)$$

and:

$$\sigma = \frac{P_0 - P_v}{\frac{1}{2} \rho_l U^2} \quad (15)$$

κ is the polytropic index for the non-condensable gas inside the bubble. Re is the Reynolds number, defined as $\text{Re} = \rho_l U R_0 / \mu_E$, where μ_E is the effective viscosity. We is the Weber number, defined as $\text{We} = \rho_l U^2 R_0 / S$, where S is the surface tension.

To solve the unknowns in equation (10) (11) and (14), appropriate initial and boundary conditions are demanded. The

number and size of the initial bubble cloud at a specific instance are extracted from the RANS results as the input. The time-dependent boundary condition at the surface cloud can be written as:

$$C_p(A(t), t) = C_{p_\infty}(t) + \frac{2}{A(t)} \frac{d[A^2(t)u(A(t), t)]}{dt} - u^2(A(t), t) \quad (16)$$

Where $C_{p_\infty}(t) = (P_\infty - P_0) / \frac{1}{2} \rho_l U^2$ is retrieved from the RANS results.

3. 2D NUMERICAL RESULTS

To get a better understanding of the steady and unsteady cavitation phenomena, thorough studies are conducted on the NACA0015 hydrofoils with an angle of attack (AoA) of 6 deg and 8 deg respectively.

The first case to be studied is a NACA0015 hydrofoil with an angle of attack of 6 deg with a chord length $C = 200\text{mm}$, which was also a selected test case in the Virtue_WP4 Workshop. The size of the computational domain is $1400 \times 570\text{mm}$, extending 2 chord lengths ahead of the leading edge and 4 chord lengths behind the trailing edge. Two conditions are simulated: a non-cavitating condition, and a cavitating condition at $\sigma = 1.0$. This latter case is expected to give unsteady cavitation with cyclic shedding. Another case is conducted on a NACA0015 hydrofoil with an angle of attack of 8 deg with a chord length $C = 60\text{mm}$. Experimental data for this case has been provided by the CRS Erosion II Project. The size of the computational domain is $570 \times 80\text{mm}$, extending 3 chord lengths ahead of the leading edge and 5.5 chord lengths behind the trailing edge. Two conditions are simulated: a non-cavitating condition and an unsteady cavitating condition at $\sigma = 2.2$. The grids for both angles of attack are block-structured grids consisting of an O-grid around the hydrofoil, embedded in an H-grid (12 blocks).

A fully coupled solver is selected to solve the pressure and momentum equations, which can lead to a more robust calculation and faster convergence [6]. A velocity-inlet boundary condition is applied on the upstream inflow with the vapor volume fraction equaling to zero. On the outlet boundary, a pressure-outlet boundary condition is used, so that the cavitation number can be derived from the specified pressure at the outlet. The discretization schemes adopt QUICK in space, PRESTO! for pressure and first order implicit in time. The detailed boundary conditions and the physical properties of the flow for these cases are listed in Table 1.

Table 1: Boundary conditions and flow properties

Boundary conditions	AoA 6		AoA8	
Inflow: Velocity Inlet (m/s)	U=6		U=17.71	
Outflow: Pressure Outlet (Pa)	20900		346400	
Turbulent Intensity (%)	1			
Turbulent Viscosity Ratio	10			
Foil	No-slip Wall			
Tunnel Wall	Slip Wall		No-slip Wall	
Flow Properties	Vapor	Liquid	Vapor	Liquid
Density (kg/m3)	0.023	998	0.01389	998.85
Dynamic Viscosity (kg/ms)	9.95E-06	0.0011	9.63E-06	0.0011
Vapor Pressure (Pa)	2970		1854	

3.1 NON-CAVITATING CONDITION

For the non-cavitating flow, the results from XFOIL including viscous effects are provided to give a comparison. For the hydrofoil with the angle of attack of 6 deg. the results obtained from FLUENT and XFOIL match each other very well, see Fig.2 a). In previous work [7], it is concluded that a higher lift and drag coefficient and a lower minimum pressure coefficient are predicted by FLUENT with a smaller bounded domain as compared to XFOIL. Similarly, due to the wall effects caused by the smaller domain in the vertical direction, the flow characteristics of the hydrofoil with an angle of attack of 8 deg, predicted by FLUENT, show a lower minimum pressure coefficient than the values obtained by XFOIL, see Fig.2 b). The values of the integrated forces and the minimum pressure coefficients predicted by FLUENT and XFOIL are listed in the Table 2, confirming the conclusion of the previous work [7]. The contours of the velocity magnitude for the NACA0015 hydrofoil at two different angles of attack are shown in the Fig.3. It is interesting to see that a larger separation zone can be observed for the hydrofoil at a higher angle of attack, implying that stronger dynamics are expected.

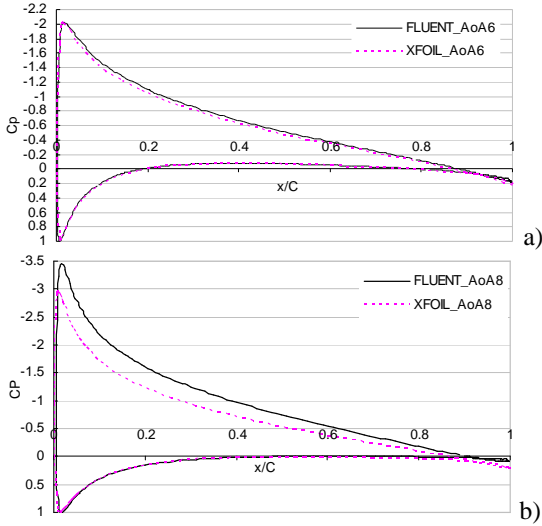


Figure 2: The pressure distribution along the NACA0015 hydrofoil at different angle of attack: a) AoA 6; and b) AoA 8

Table 2: Flow characteristics for NACA0015 hydrofoils

Flow Characteristics	AoA 6		AoA8	
	FLUENT	XFOIL	FLUENT	XFOIL
Lift Coefficient (CL)	0.659	0.6563	1.03698	0.8669
Drag Coefficient (CD)	0.01415	0.01341	0.01797	0.01479
Minimum Pressure Coefficient (Cpmin)	-2.0581	-2.0487	-3.4682	-2.993

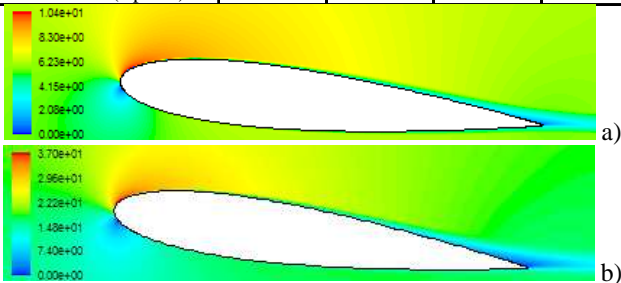


Figure 3: Contours of the velocity magnitude of NACA0015 hydrofoil at different angles of attack: a) AoA 6 deg; and b) AoA 8 deg

3.2 UNSTEADY CAVITATING CONDITION

A characteristic phenomenon associated with extended sheet cavitation is its break-up behavior, leading to the shedding of patches of cavitation. It is however not trivial that this shedding phenomenon is found from a multiphase CFD code. Reboud et al [2] were amongst the first to conclude this and proposed a procedure to attenuate the eddy viscosity at the vapor-liquid interface (Reboud et al. [1998]). Also with the RANS code FLUENT, the break-up of the sheet cavity and corresponding periodic shedding of the cloud cavity at the trailing edge of the sheet can only be predicted by an artificial reduction of the turbulence viscosity in the regions of higher vapor volume fraction [7-9]. A study of this effect will be reported in this section. It should however be noted that the modification of the turbulence model based on the idea of Reboud et al [2] is not a prerequisite for shedding for all commercial CFD tools [10-11].

According to the non-cavitating results, the inception cavitation number of the hydrofoil with 6 deg AoA is much lower than that of the hydrofoil with 8 deg AoA. For the NACA0015 hydrofoil with 6 deg AoA, the investigation is conducted at $\sigma = 1.0$ in order to obtain unsteady cyclic shedding. The time step size is chosen as $\Delta t = 5e-04$ according to a dimensionless time $\Delta t^* = \Delta t U / C = 0.015$. According to the experimental data, the NACA0015 hydrofoil with 8 deg AoA already reveals unsteady cavity dynamics at $\sigma = 2.2$. The time steps chosen here are $\Delta t = 5e-04$ and $\Delta t = 5e-05$. The latter time step is in agreement with the same non-dimensional time as the case for the 6 deg AoA.

3.2.1 UNSTEADY PHENOMENA WITH AOA 6

As mentioned above, only a back-and-forth oscillating sheet cavity is observed with the standard $SST k - \omega$ turbulence model, whereas an unsteady sheet with shedding behavior was expected based on earlier results [8, 10-11]. For simulations where convergence is certainly satisfied, the necessity of the eddy viscosity correction as proposed by Reboud et al [2] is examined. Potential factors that may cause the lack of compliance with the expected realistic physics are investigated, such as the grid sensitivity, bubble number density and higher orders of the temporal discretization scheme. After unsuccessful endeavors, the sheet cavity still does not show a tendency of breaking-up and shedding. Instead, the sheet cavity shows a “breathing” behavior, reaching a maximum cavity length of approx. 43% chord and a minimum cavity length of approx. 20% chord, see Fig.4. The contours of the vapor volume fraction at the typical peak and trough of the total vapor volume are shown in Fig.5.

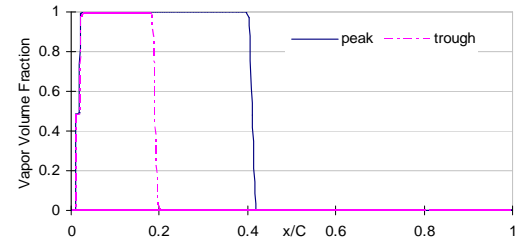


Figure 4: Vapor volume fraction distribution over a NACA0015 hydrofoil with 6 deg AoA at the peak and trough of the total vapor volume at $\sigma = 1.0$ with standard $SST k - \omega$ model

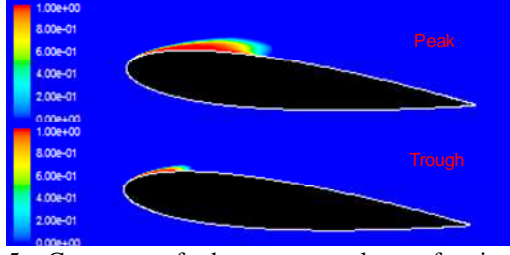


Figure 5: Contours of the vapor volume fraction for a NACA0015 hydrofoil with 6 deg AoA at the peak and trough of the total vapor volume at $\sigma = 1.0$ with standard $SST k - \omega$ model

Unsteady cavitation dynamics are only triggered after Reboud's modification for the eddy viscosity in the region of the vapor-liquid interface is applied. In this case, the periodic shedding of the cloud cavity at the trailing edge after break-up of the sheet cavity occurs with a natural frequency of 3.5 Hz with the default iteration numbers per time step. This is in disagreement with results reported by Koops [12] on a similar study on the NACA0015 foil, where he found frequencies ranging from 11Hz to 24Hz. After close examination, an insufficient number of iterations per time step is found to be the cause of the underestimation of the shedding frequency. It is found that the default number of 20 iterations per time step is indeed inadequate to attain a converged mass transfer rate and a sound residual behavior, see Fig.6.

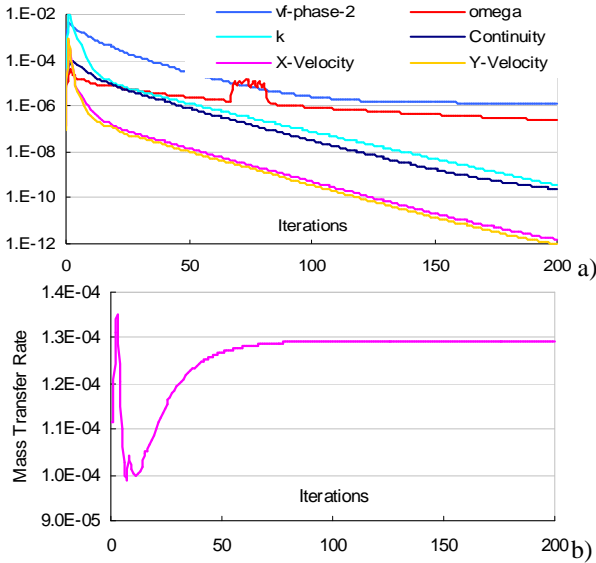


Figure 6: The behavior of the a) scaled residuals and b) integrated mass transfer rate during one time step

After a sensitivity study for the number of iterations using FFT analysis to study the frequency content, it is found that the preferable cyclic shedding at a natural frequency of around 14 Hz can be obtained by increasing the default 20 iterations per time step to a number of 100 iterations. The images shown in Fig. 7 are predicted by the adequate iterative solutions, clearly describing the essential features of the unsteady shedding in a typical cycle. At first, a sheet cavity is growing from the leading edge after the last cavity pinch-off (see Fig.7 a); A re-entrant jet forms subsequently and moves upstream towards to the leading edge (Fig.7 b); The sheet cavity is then broken up by the re-

entrant jet (Fig.7 c); The upstream part of the sheet cavity subsequently decreases to a very tiny volume, whereas the downstream part rolls up and transforms into a bubbly cloud (Fig.7 d and e); Finally, the cloud cavity is lifted from the foil surface and collapses downstream in the vicinity of the trailing edge. Then a tiny sheet cavity from the leading edge grows again and a new cycle starts (Fig.7 f).

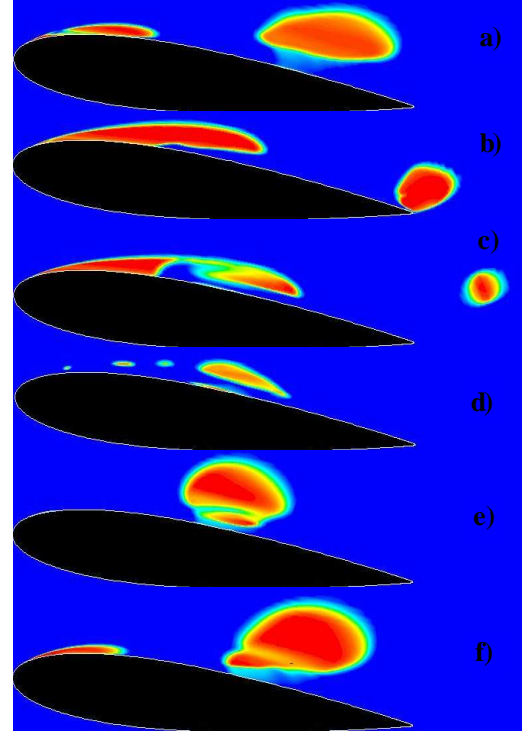


Figure 7: Contours of the total vapor volume over a NACA0015 hydrofoil (AoA 6) within a typical shedding cycle

3.2.2 UNSTEADY PHENOMENA WITH AOA 8

At first, the time step size of $\Delta t = 5e - 04$ is used to explore the cavitating flow over the NACA0015 hydrofoil with angle of attack of 8 deg at a cavitation number $\sigma = 2.2$. Without the modification of the turbulence model, only a steady sheet cavity is observed with a length of 12.5% of the chord, see Fig.8.

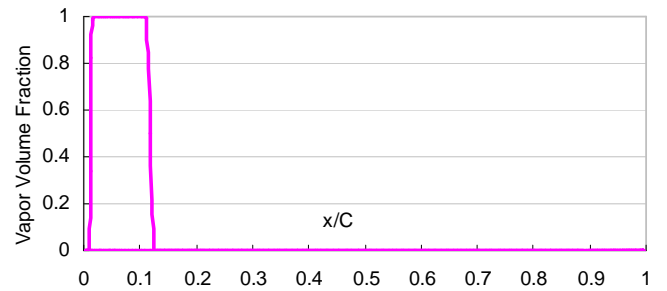


Figure 8: Volume fraction distribution over a NACA0015 hydrofoil with angle of attack of 8 deg

When the modified $SST k - \omega$ turbulence model is applied, more repeatable unsteady dynamics, the break-up of the sheet cavity and the shedding of cloud cavities, can be observed. This is contrast to a seemingly random behavior predicted for the case with a 6 deg angle of attack. The time histories of the lift coefficient versus time after subtracting the start-up time are shown in the Fig.9.

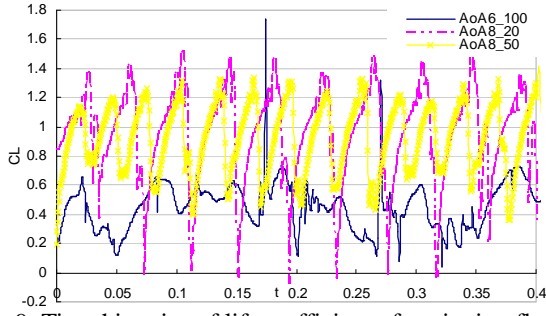


Figure 9: Time histories of lift coefficient of cavitating flow over NACA0015 hydrofoils at 6 deg and 8 deg angle of attack. Two different iteration numbers per time step are plotted for the 8 deg AoA case (i.e. 20 and 50 iterations)

In line with the analysis carried out in the previous case, an investigation on the iteration numbers per time step is conducted to assure convergence of the solutions. The behavior of the residuals and integrated mass transfer indicate that 50 iterations per time step are demanded. Upon a spectral analysis of the convergence history of the total vapor volume predicted by the two different iteration numbers per time step, the number of 50 iterations shows a higher frequency than the number of 20 iterations (33 Hz versus 25.6 Hz respectively). Fig.10 shows the results from the spectral analysis and also shows the differences in power spectral density for the two different iteration numbers.

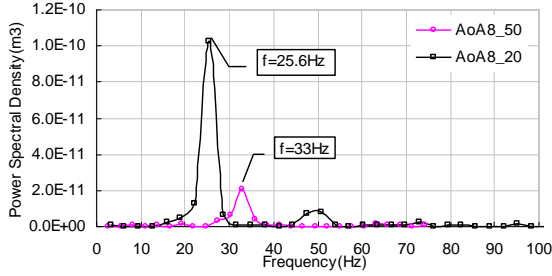


Figure 10: The spectral analysis of convergence history of the total vapor volume predicted by different iterations per time step

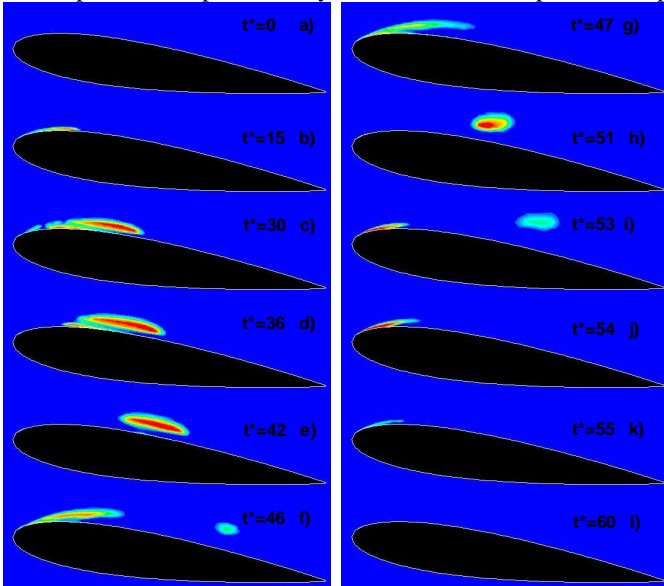


Figure 11: Contours of vapor volume fraction over a NACA0015 hydrofoil with angle of attack of 8 deg during one typical cycle with $\Delta t = 5e - 04$

During one typical cycle, two types of shedding are predicted as shown in Fig.11. The first shedding accounts for the first three quarters of the whole cycle (Fig.10 a-f), and the second shedding occurs in the subsequent time period (Fig.10 g-l). The time t^* indicates the dimensionless time $t^* = (t - t_0) / \Delta t$.

To be consistent with the dimensionless time step size, $\Delta t^* = \Delta t U / C = 0.015$, adopted by the previous case with the angle of attack of 6 deg, a time step size of $\Delta t = 5e - 05$ is taken. This smaller time step subsequently resulted in different cavity dynamics. The cavity that breaks up from the sheet cavity is shed at a high frequency with a cyclic variation of the magnitude of the total vapor volume for the lower frequency. The unsteady cavity dynamics only appear at the front part of the hydrofoil due to the diminished total vapor volume. It is observed that there are a dozen of high-frequency oscillations during each typical cycle, as shown in Fig.12. Two groups of images are shown in Fig.13 to represent the cavitating phenomena corresponding to oscillations with a minimum and maximum magnitude of the total vapor volume.

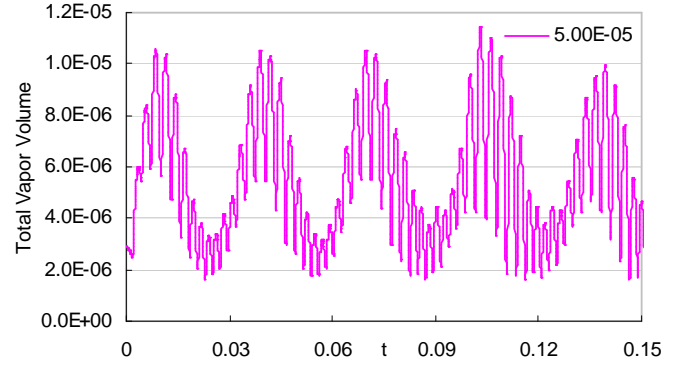


Figure 12: The time history of the total vapor volume obtained with the time step size $\Delta t = 5e - 05$

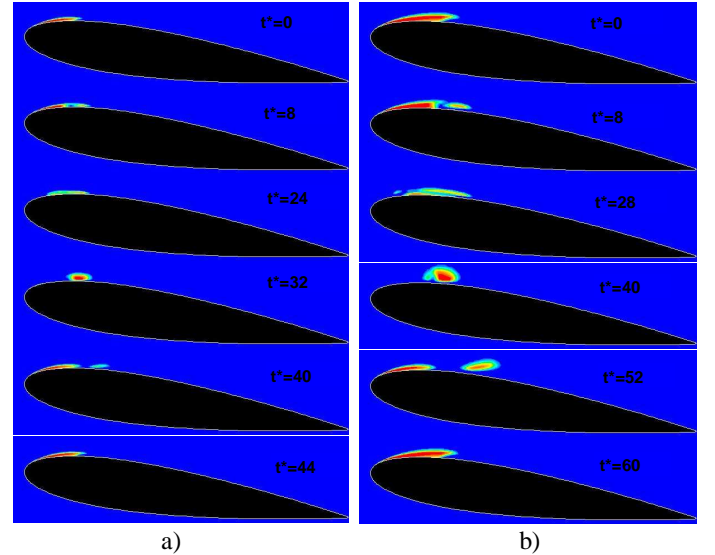


Figure 13: Two groups of contours of the vapor volume fraction over a NACA0015 hydrofoil with angle of attack of 8 deg during one typical cycle with $\Delta t = 5e - 05$, respectively corresponding to the oscillation with a) minimum and b) maximum magnitude of the total vapor volume

It is assumed that this remarkable discrepancy between the dynamics predicted by these two time step sizes may be due to the temporal sensitivity. A further study on this aspect is demanded.

4. 3D NUMERICAL RESULTS

After examination of the 2D cases, the test case is extended to the same foil in 3D. The mesh is obtained by extruding the 2D mesh generated for the NACA0015 hydrofoil at 8 deg angle of attack in the span-wise direction by 40mm, which is consistent with the set-up in the experiments carried on in the MARIN high speed cavitation tunnel. The boundary conditions are listed in Table 3.

Table 3: Boundary conditions in 3D case

Boundary conditions	3D NACA0015 (AoA8)
Inflow: Velocity Inlet (m/s)	U=17.71
Outflow: Pressure Outlet (Pa)	346400
Turbulent Intensity (%)	1
Turbulent Viscosity Ratio	10
Foil	No-slip Wall
Tunnel Bottom and Ceiling	No-slip Wall
Tunnel Side Walls	Symmetry

4.1 CAVITATION PHENOMENA

The time history of the total vapor volume and the corresponding spectral analysis result are shown in Fig.14.

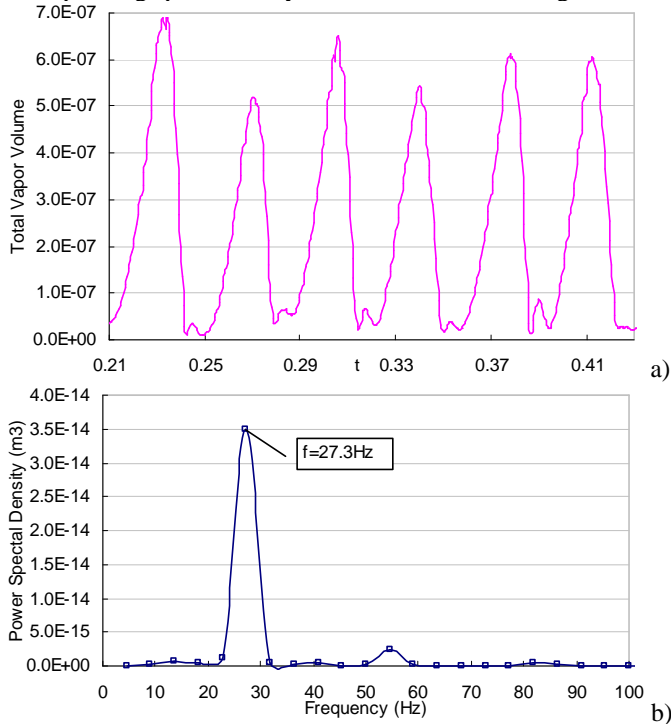


Figure 14: a) The time history of the total vapor volume; and b) its spectral analysis

The typical images obtained by visualizing the iso-surface of the instantaneous volume fraction of $\alpha=0.1$ are shown in Fig.15, representing a typical shedding cycle. The main sheet cavity develops from the leading edge (Fig.15 a); re-entrant jet forms and moves to the leading edge, and breaks up the main sheet cavity (Fig.15 b); the shed cavity moves downstream and collapses close to one sidewall around mid-chord (Fig.15 c); a

second cloudy cavity sheds from the sheet cavity due to a newly developed re-entrant jet occurring at the span-wise position of the first imploded cavity (Fig.15 d-e); both shed cavities collapse and the main sheet cavity starts to develop again without further shedding behavior (Fig.15 f-g); The main sheet cavity shrinks to a minimum volume and then a new cycle starts (Fig.15 h).

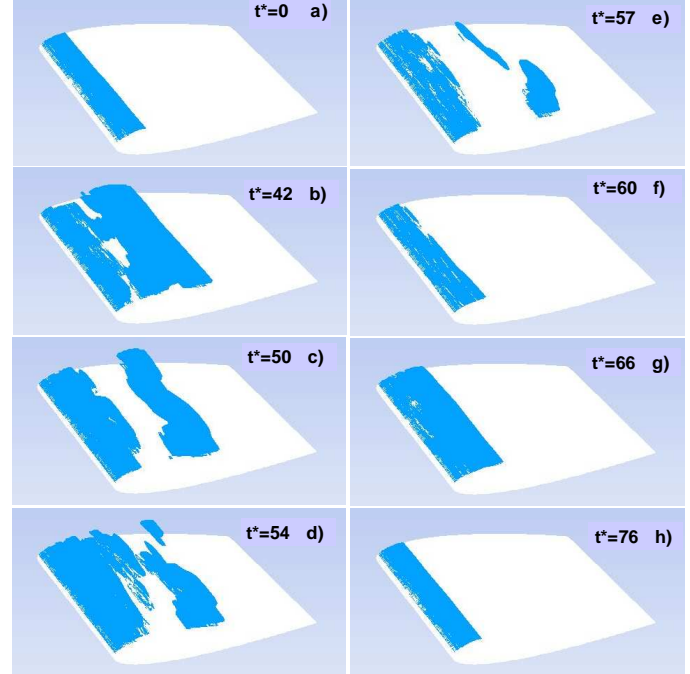


Figure 15: Sequence of iso-surface plots of the instantaneous volume fraction of $\alpha=0.1$ during one typical shedding cycle on the NACA0015 hydrofoil (3D representation) with an angle of attack of 8 deg at $\sigma=2.2$

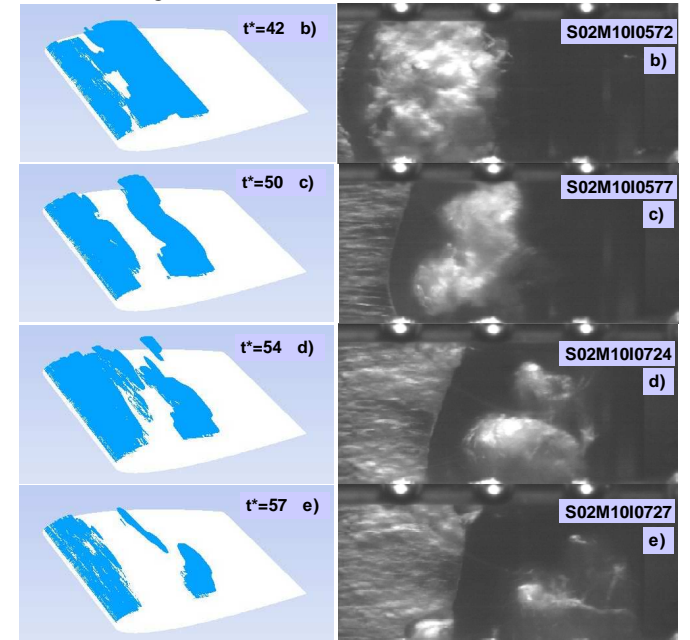


Figure 16: Four characteristic frames recorded by high-speed camera corresponding to the four instants shown in Fig.15 b)-e)

The predicted mean cavity length is about 50% of the chord, which is very close to the 48% chord measured from the experiments [13]. Four characteristic frames recorded by the high-speed camera are shown in Fig.16. Though the corresponding dynamics predicted by the current RANS code is not entirely identical to the experimental results, it can still be concluded that the main unsteady shedding features are successfully captured by the RANS code. Regarding the numerical instability issues encountered in 2D cases, the 3D results are also demanding further investigations on the temporal sensitivity issues.

4.2 IMPACT PRESSURE FROM RANS CODE

From an energy consideration, it is suggested here that the focusing of potential energy in a macro cavity may produce high values of the impact loads, which are supposed to be related to the impulsive pressure pulses produced during the collapse process. Figure 17 shows the contours of the instantaneous static pressure distribution on the suction side, corresponding to the instants revealing the focusing and collapsing as depicted in Fig.15. It is shown that at the end of the collapse process, high pressure impacts can be observed ($t^*=60$). At first instance, around the trailing edge where a peak pressure of the order of 4×10^5 Pa is noted. A slightly smaller pressure is observed at the collapsing center of the first shed cavity of 3×10^5 Pa. These impact loads for an 8 deg angle of attack are ten times higher than the values obtained from the results of 3D NACA0015 hydrofoil at 6 degree angle of attack [7].

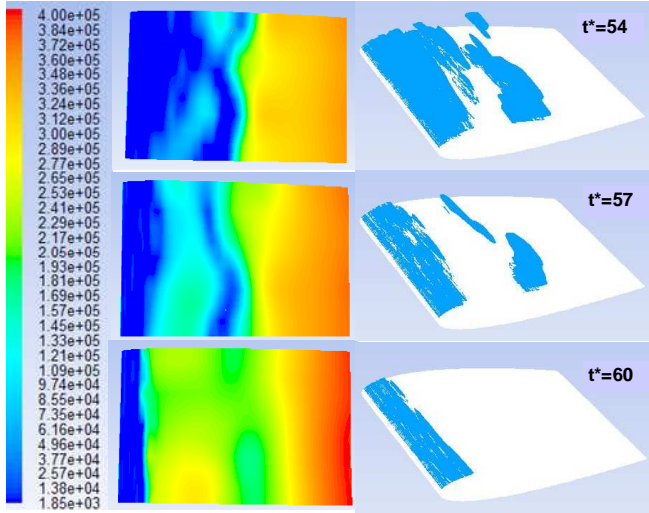


Figure 17: Contours of the instantaneous static pressure (in Pa) distribution on the suction side corresponding to three selected instants in Fig.15

4.3 EROSION ASSESSMENT

Although the above evaluation of the RANS results offers a possibility to assess the risk of cavitation erosion by the pressure impacts on the foil surface, much more details accounting for the micro-scale mechanisms are likely needed to give a reliable quantitative assessment. Therefore, an energy approach has been studied, using a numerical model proposed by Wang and Brennen [3]. This model is studied as a postprocessor for a quantitative relation between the numerical results by the unsteady RANS code and the risk of cavitation erosion.

It is hypothesized that the most important mechanism for cavitation erosion consists of the acoustic shock waves that are released upon the violent collapse of cloudy cavities near the solid surface (Van Terwisga et al. [14]). What we can observe from the unsteady two-phase RANS code is limited to the large scale dynamics. To bridge the gap between the RANS results and the prediction of the erosion risk, the bubble cloud collapse model proposed by Wang and Brennen [3] is adopted to provide more details on the collapse mechanism.

At first, due attention should be paid to choose the appropriate results from the RANS code as input into the bubble cloud model. The initial input parameters should be scrupulously translated to provide a quasi equivalent bubble cloud. Then, a pressure perturbation $C_{p\infty}(t=0)$, corresponding to the pressure field at the same specific instant from the RANS results, is imposed on the pure liquid at infinity and the response of the cloud to this pressure perturbation is taken for a more elaborate view of the collapse of the cloudy bubble cluster. The surrounding pressure will vary in some way because the assumed bubble cloud travels downstream during its collapse. However, as regard to the very short period of time, this discrepancy of the ambient pressure is neglected.

Subsequently, the radiated acoustic pressure in the far field can be calculated by the volumetric acceleration of the cloud. The normalized far-field acoustic pressure is calculated as:

$$P_a(t) = \frac{2R_0}{D} \left[A^2(t) \frac{d^2 A(t)}{dt^2} + 2A(t) \left(\frac{dA(t)}{dt} \right)^2 \right] \quad (17)$$

Where R_0 is the initial bubble radius, D is the length scale and A is the radius of the bubble cloud

The first attempt of application of this methodology has been reported already done by Van Loo [15] and shows the possibility to make a quantitative evaluation of the radiated acoustic energy. Further study and validation with the experimental measurements are in progress.

5. CONCLUSIONS AND RECOMMENDATIONS

The multiphase RANS code FLUENT 12.0 is investigated on NACA0015 hydrofoil at 6 and 8 degrees angle of attack in both 2D and 3D in order to assess its capability to capture the unsteady cavitating phenomena and subsequently the possibility to make an assessment of the risk of cavitation erosion.

Important conclusions are:

1. A realistic dynamic shedding of the sheet cavitation is only obtained after attenuating the eddy viscosity in the region with higher vapor volume fraction in the multiphase RANS code FLUENT.
2. It should be noted that for the unsteady simulations, the number of iterations per time step should be carefully selected in order to avoid lack of numerical convergence, which may result in a significant influence on the prediction of the shedding frequency and the magnitude of the total vapor volume.
3. A tentative analysis of the correlation between the pressure impacts and the unsteady collapsing phenomena gives promise to the prediction

capability of the most probable locations for cavitation erosion damage.

4. An additional cavity cloud collapse model due to Wang and Brennen (1999) where RANS results are used as input is proposed. This model would provide more details on the collapse mechanism and would allow for a more quantitative criterion. However, further testing of the suitability of this model in conjunctions with unsteady RANS is demanded.

ACKNOWLEDGMENTS

The authors are grateful for the reports of the experiments on the NACA0015 hydrofoil provided by the Cooperative Research Ships (CRS), administered by MARIN. Experimental data on the NACA0015 hydrofoil have been made available by the Cavitation Erosion Project of CRS. The authors are also grateful for the contribution by Sebastiaan Van Loo for his work on the Wang and Brennen (1999) model.

REFERENCES

- [1]Bark, G, Berchiche, N. and Grekula, M. (2004). 'Application of principles for observation and analysis of eroding cavitation – The EROCAV observation handbook', Edition 3.1
- [2]Reboud J L, Stutz B and Coutier O. (1998). 'Two phase flow structure of cavitation experiment and modeling of unsteady effects'. Proc. of the 3rd Int. Symp. on Cavitation, Grenoble, France.
- [3]Wang, Y-C and Brennen, C.E. (1999). 'Numerical computation of shock waves in a spherical cloud of cavitation bubbles,, Journal of Fluids Engineering
- [4]Menter F.R. (1994). 'Two-Equation Eddy-viscosity Turbulence Models for Engineering Applications'. AIAA Journal, 32(8), pp. 1598-1605.
- [5]Schnerr, G. H. & Sauer, J. (2001). 'Physical and Numerical Modeling of Unsteady Cavitation Dynamics'. 4th Int. Conf. on Multiphase Flow, Orleans, USA.
- [6]ANSYS FLUENT 12.0 Theory Guide, (2009).
- [7]Li, Z.R and Van Terwisga, T.J.C. (2011). 'On the capability of multiphase RANS codes to predict cavitation erosion', 2nd International Sym. on Mariner Propulsors, SMP 2011, Hamburg, Germany.
- [8]Li, D.Q, Grekula, M. and Lindell, P. (2009). 'A modified SST $k-\omega$ model to predict the steady and unsteady sheet cavitation on 2D and 3D hydrofoils'. Proc. of the 7th Int. Symp. On Cavitation, Ann Arbor, Michigan, USA.
- [9]Li, Z.R., Pourquie, M and Van Terwisga, T.J.C. (2010). 'A numerical study of steady and unsteady cavitation on a 2D hydrofoil'. 9th International Conference on Hydrodynamics, Shanghai, China.
- [10]Hoekstra, M, and Vaz, G. (2008). 'FreSCo Exercises for NACA0015 Foil'. VIRTUE WP4-Workshop II, INSEAN, Rome, Italy.
- [11]Oprea, Iulia. and Bulten, Norbert. (2009). 'RANS simulation of a 3D sheet-vortex cavitation'. Proc. of the 7th Int. Symp. On Cavitation, Ann Arbor, Michigan, USA.
- [12]Koop, A. (2008). 'Numerical simulation of unsteady 3D sheet cavitation'. PhD Thesis, University of Twente, Enschede, The Netherlands.
- [13]Report of CRS Erosion II WG. (2010) 'Task 2.3- Cavitation tests pm a NACA0015 Aerofoil: Quantification of cavitation impacts from high speed video and AE signals', TID/6997b, November.
- [14] Van Terwisga, T., Fitzsimmons, P.A., Foeth, E.J., and Li, Z.. (2009). 'Cavitation Erosion – A critical review of physical mechanisms and erosion risk models', Proceedings of CAV 2009 Conference, Ann Arbor, USA, Sept.
- [15]Sebastiaan, Van Loo. (2011). 'Numerical study on the collapsing behavior of a spherical cloud of cavitation bubbles', MSc Thesis, University of Twente, March.